

JGR Space Physics



REVIEW ARTICLE

10.1029/2021JA030214

Key Points:

- Electromagnetic ion cyclotron waves effectively scatter ultra-relativistic electrons in the radiation belts
- The local acceleration produces acceleration from MeV to multi-MeV in the regions of low density
- The difference between MeV and multi-MeV electrons justifies the classification of these particles into a new population

Correspondence to:

Y. Y. Shprits,
yshprits@gfz-potsdam.de

Citation:

Shprits, Y. Y., Allison, H. J., Wang, D., Drozdov, A., Szabo-Roberts, M., Zhelavskaya, I., & Vasile, R. (2022). A new population of ultra-relativistic electrons in the outer radiation zone. *Journal of Geophysical Research: Space Physics*, 127, e2021JA030214. <https://doi.org/10.1029/2021JA030214>

Received 16 DEC 2021

Accepted 4 APR 2022

Author Contributions:

Conceptualization: Yuri Y. Shprits
Data curation: Yuri Y. Shprits
Formal analysis: Yuri Y. Shprits, Hayley J. Allison, Dedong Wang
Funding acquisition: Yuri Y. Shprits
Investigation: Yuri Y. Shprits
Methodology: Yuri Y. Shprits
Project Administration: Yuri Y. Shprits
Resources: Yuri Y. Shprits, Matyas Szabo-Roberts, Irina Zhelavskaya
Software: Yuri Y. Shprits
Supervision: Yuri Y. Shprits
Validation: Yuri Y. Shprits
Visualization: Yuri Y. Shprits
Writing – original draft: Yuri Y. Shprits
Writing – review & editing: Yuri Y. Shprits, Hayley J. Allison, Dedong Wang, Alexander Drozdov, Ruggero Vasile

© 2022. The Authors.

This is an open access article under the terms of the Creative Commons Attribution-NonCommercial-NoDerivs License, which permits use and distribution in any medium, provided the original work is properly cited, the use is non-commercial and no modifications or adaptations are made.

A New Population of Ultra-Relativistic Electrons in the Outer Radiation Zone

Yuri Y. Shprits^{1,2,3} , Hayley J. Allison¹ , Dedong Wang¹ , Alexander Drozdov² , Matyas Szabo-Roberts^{1,2} , Irina Zhelavskaya¹ , and Ruggero Vasile¹

¹GFZ German Centre for Geosciences, Potsdam, Germany, ²Department of Earth, Planetary, and Space Science, University of California, Los Angeles, Los Angeles, CA, USA, ³Institute of Physics and Astronomy, University of Potsdam, Potsdam, Germany

Abstract Van Allen Probes measurements revealed the presence of the most unusual structures in the ultra-relativistic radiation belts. Detailed modeling, analysis of pitch angle distributions, analysis of the difference between relativistic and ultra-realistic electron evolution, along with theoretical studies of the scattering and wave growth, all indicate that electromagnetic ion cyclotron (EMIC) waves can produce a very efficient loss of the ultra-relativistic electrons in the heart of the radiation belts. Moreover, a detailed analysis of the profiles of phase space densities provides direct evidence for localized loss by EMIC waves. The evolution of multi-MeV fluxes shows dramatic and very sudden enhancements of electrons for selected storms. Analysis of phase space density profiles reveals that growing peaks at different values of the first invariant are formed at approximately the same radial distance from the Earth and show the sequential formation of the peaks from lower to higher energies, indicating that local energy diffusion is the dominant source of the acceleration from MeV to multi-MeV energies. Further simultaneous analysis of the background density and ultra-relativistic electron fluxes shows that the acceleration to multi-MeV energies only occurs when plasma density is significantly depleted outside of the plasmasphere, which is consistent with the modeling of acceleration due to chorus waves.

Plain Language Summary The most energetic electrons in the Earth Van Allen radiation belts have not been accurately measured in the past. Observations for a recent NASA's Van Allen Probes missions reviled new unique structures, such as narrow rings, and posed further scientific questions. This review shows that, unlike relativistic electrons, ultra-relativistic electrons can be very effectively locally scattered by plasma waves produced by ions, so-called electromagnetic ion cyclotron waves. Observations also show that acceleration from MeV to multi-MeV occurs locally by taking energy from another type of plasma wave. These waves are called whistler-mode waves and can accelerate particles to such high energy when total plasma density is low. The difference between the relativistic and ultra-relativistic particles justifies the classification of these particles into a different population from the bulk population of the outer radiation belt.

1. Introduction

Recent decades have seen an increased interest in radiation belt research. Inspired by the detailed measurements of the Combined Release and Radiation Effects (CRRES) satellite in 1990–1991, research focused on the quantification of acceleration and loss mechanisms and preparation for NASA's Radiation Belt Storm Probes (RBSPs) mission; renamed by NASA after the successful launch on August 30, 2012, to Van Allen Probes. Even before the launch of the Van Allen Probes mission, increased interest in radiation belt physics resulted in the identification of several acceleration and loss mechanisms and quantification of the wave-particle interaction and transport of electrons in the radiation belts. The historical static picture of the radiation belts explained by Lyons and Thorne (1973), where the belt structure has been modeled as a steady-state balance of acceleration by radial diffusion and loss due to hiss waves, has been revisited. While the static model of Lyons and Thorne (1973) could successfully reproduce the structure of the belts during quiet conditions, during storms, the belts show considerable variability and cannot be described by a steady-state model (Shprits & Thorne, 2004). Erosion of the plasmasphere allows chorus waves to effectively resonate with relativistic electrons and produce scattering (Thorne et al., 2005) as well as acceleration (Horne & Thorne, 1998; Summers et al., 1998). Further modeling efforts allowed us to quantify the scattering rates outside of the plasmasphere (Albert, 2005; Glauert & Horne, 2005; Horne et al., 2005; Shprits & Ni., 2009). Observational efforts showed evidence of the peaks in phase space density (PSD) observed on Polar and the CRRES missions that were indicative of the local

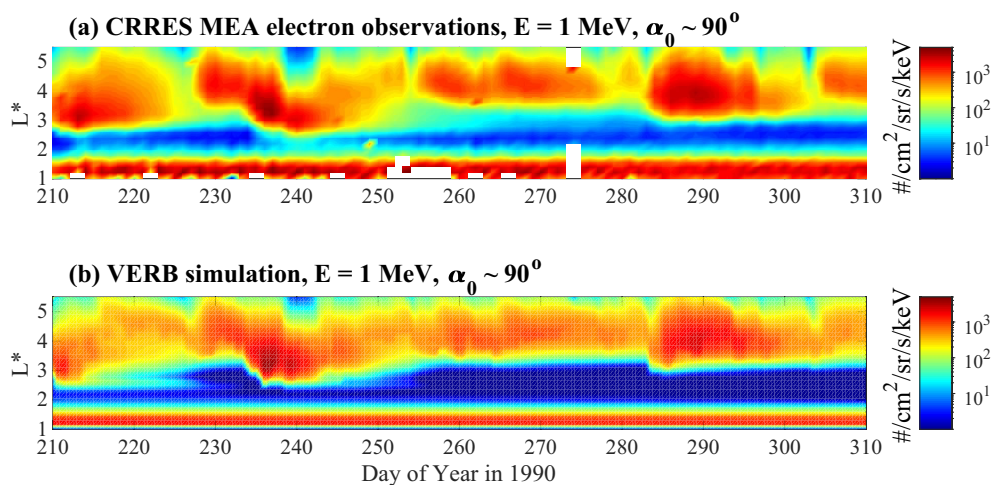


Figure 1. Comparison of the VERB-3D code simulations and CRRES observations. (a) 1 MeV MEA electron flux observed on CRRES and (b) VERB code simulations using only observations at $L = 5.5$ and Kp index (Adopted from Kim et al., 2011).

acceleration by chorus waves (Y. Chen et al., 2007; Green & Kivelson, 2004; Iles et al., 2006). Modeling the dynamics of fluxes has also been revisited, and time dependence was introduced (Shprits & Thorne, 2004) into what was previously considered as a steady-state radial diffusion model. Long-term simulations with a radial diffusion code showed that radial diffusion is capable of reproducing the structure of the radiation belts (Shprits et al., 2005). These simulations helped reveal another very important loss mechanism that provides a dominant loss of electrons during storms and explains dramatic non-adiabatic electron depletion events, known as dropouts, in the belts. The correlation of dropouts, for a wide range of energies from 100s of keV to MeV, with increases in the solar wind dynamic pressure, as well as the effects of the variable outer boundary in long term simulations, indicated that main phase dropouts are produced by outward radial diffusion that is driven by loss to the magnetopause (Shprits, Thorne, Friedel, et al., 2006). Further observational evidence for this loss mechanism came from the measurements on the National Oceanic and Atmospheric Administration (NOAA) POES spacecraft, which showed no evidence of 100s of keV electrons precipitating into the atmosphere during storms, confirming that the most plausible mechanism for the loss of these particles is the outward radial diffusion driven by the loss to the magnetopause (Turner et al., 2012). These improvements in the understanding of relativistic electron dynamics translated into improvements in modeling. The Versatile Electron Radiation Belt (VERB) model could account for all of these physical processes, including pitch angle and energy scattering, and loss to the magnetopause (Shprits et al., 2008, 2009). With the addition of mixed diffusion (Albert & Young, 2005), the VERB code was able to qualitatively reproduce the dynamics of the belts, as observed by the CRRES satellite (Subbotin et al., 2010). Figure 1 shows an example of such simulations of 100 days in the year 1990 (Kim et al., 2011). By utilizing measurements only at the outer boundary along with the values of the Kp index, the code was capable of reproducing the inward extent of the outer radiation belt flux, the peak fluxes, the variations of fluxes near GEO, and the general dynamics of the belts.

A number of codes (Glauert et al., 2014, 2018; Ma et al., 2015, 2018; Ma, Li, Thorne, Bortnik, et al., 2016; Ma, Li, Thorne, Nishimura, et al., 2016; Ripoll et al., 2016, 2019; Su et al., 2014; Tu et al., 2013; Varotsou et al., 2008) used a similar methodology to VERB, in particular the chosen boundary conditions and the two-grid approach (Subbotin & Shprits, 2009).

The scientific findings described above, validated by physics-based models on long-term data sets, implied that the most dominant mechanisms related to the dynamics of the belts had been quantified and well-understood even before the launch of the Van Allen Probes mission. The mission was expected to provide more detailed evidence of the already established mechanisms and better quantify the wave and particle environment. The results from the mission certainly surprised researchers by revealing so many new morphological structures and physical mechanisms. Examples of such findings include observing an absence of >800 keV electrons in the inner belt (Fennel et al., 2015), finding and explaining the zebra stripes (Ukorskiy et al., 2014), and identifying narrow

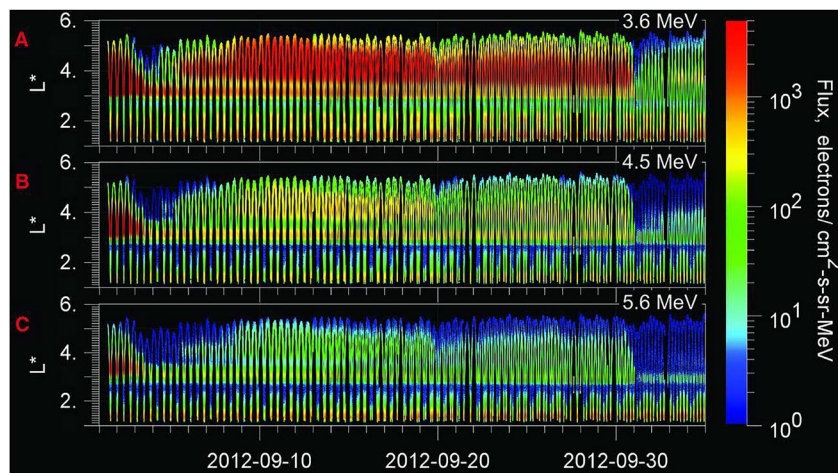


Figure 2. Van Allen Probes REPT measurements of fluxes as a function of L^* and time for September 1 to October 4, 2012. Electron differential flux is color-coded as a logarithmic scale. (a) Radiation belt electrons with kinetic energy from 3.2 to 4.0 MeV. (b) Radiation belt electrons with kinetic energy from 4.0 to 5.0 MeV. (c) Radiation belt electrons with kinetic energies from 5.0 to 6.2 MeV (Adopted from Baker, Kanekal, Hoxie, Henderson, et al., 2013).

rings of electrons at multi-MeV energy (Baker, Kanekal, Hoxie, Henderson, et al., 2013). These observations helped reveal gaps in understanding, helped determine new physical processes, and allowed long-term global models to be further refined. Furthermore, the Van Allen Probes mission included instrumentation to reliably measure >3 MeV populations, so-called ultra-relativistic populations, for the first time. This review focuses on the improved understanding of the transport, loss, and acceleration of these ultra-relativistic electrons. We start by discussing several events from the Van Allen Probes era that allowed researchers to disentangle various acceleration and loss mechanisms and identify dominant loss mechanisms. We discuss the loss due to electromagnetic ion cyclotron (EMIC) waves and the energies affected by EMIC wave scattering in Section 2. We further proceed with analyzing the observations of the acceleration processes at ultra-relativistic energies (Section 3). The implications of the results are summarized in the discussion and conclusion (Section 4).

2. Local Loss Due to EMIC Waves

Right after the Van Allen Probes mission launch, new measurements at multi-MeV energies revealed the most unusual new structure in the outer radial zone. A very narrow remnant belt was formed on September 3, 2012, near $L = 3$, and persisted until the next storm wiped it out on September 30, 2012 (Figure 2).

The VERB-3D code, similar to the code used for the simulation in Figure 1, was able to reproduce the general dynamics of the 2 MeV flux, with a dropout and rebuilding of the belts, but was not capable of reproducing the unusual narrow belt at multi-MeV. The simulation was initiated on August 1, 2012, before the launch of the Van Allen Probes mission (see Figure 3) where the times when data was not still available are shown as black. At multi-MeV energies, the code predicted a broad intensified outer belt (Shprits et al., 2013), while observations showed a split structure of the belts with a very narrow ring between the typical outer and inner belt structures, dubbed as a “storage ring” in Baker, Kanekal, Hoxie, Batiste, et al. (2013).

These simulations indicated that the standard set of physical processes for VERB-3D, as discussed in the introduction and used for the long-term comparison with CRRES MeV fluxes, may be insufficient to explain these unusual structures at multi-MeV energies (Figure 3). The simulation with the standard set of parameters does not produce the narrow ring between the belts and just predicts a standard two zone structure.

Another potentially important mechanism of scattering of the ultra-relativistic electrons was suggested by Thorne and Kennel (1971). In this mechanism, doppler-shifted L-mode EMIC waves can resonate with relativistic electrons. Observations from GOES and the Canadian Array for Realtime Investigations of Magnetic Activity (CARISMA) stations showed that EMIC waves were present on September 2–5, 2012. By introducing the

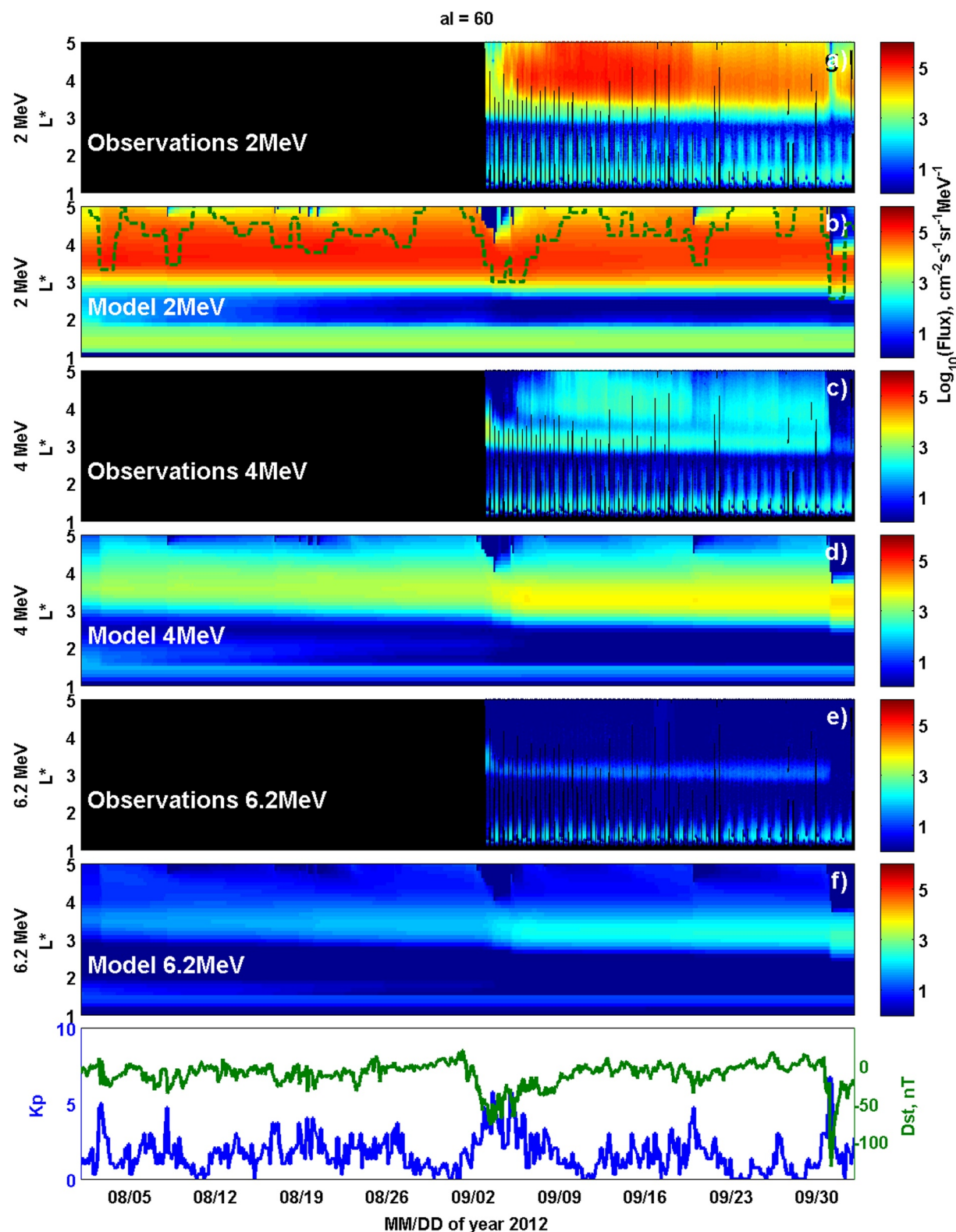


Figure 3. Comparison of observations and model results. Simulations were initiated on August 1, 2012 prior to the launch of the Van Allen Probes mission. (b, d, f) VERB simulations not including EMIC wave scattering (a, c, e) observations from the Van Allen Probes for kinetic energies $E = 2, 4$, and 6.2 MeV. Panels (a)–(f) show omni-directional electron fluxes as a function of time and L^* . Simulations failed to reproduce the unusual dynamics of the radiation belts and the formation of the long-lived, very narrow remnant belt at ultra-relativistic energies. The bottom panels show K_p and Dst indices (Adopted from Shprits et al., 2013).

diffusion coefficients describing the effect due to EMIC waves into the VERB-3D code, it was possible to reproduce the deeper dropout at multi-MeV and reproduce the formation of a very narrow remnant belt (Figure 4).

Shprits et al. (2013) showed that the inclusion of EMIC wave scattering allowed the model to reproduce a deeper dropout at multi-MeV than at MeV energies. While the outward radial diffusion loss affected all energy electrons, EMIC waves can produce localized loss at multi-MeV deeper into the heart of the belts. At multi-MeV, scattering by hiss and chorus becomes much less efficient, which allows the remnant narrow belt to persist for almost a month.

While comparing model outputs and observations is essential for guiding our understanding of acceleration and loss processes, having direct observational evidence is still most critical. Observations can also help identify when different acceleration and loss mechanisms may take place. An insight into the loss of radiation belt electrons, specifically the type of loss, location, and energies affected by the loss, may be obtained by analyzing the radial profiles of PSD for given fixed values of the first and second adiabatic invariants.

Figure 5 illustrates the dynamics of PSD for three potential types of loss in the absence of acceleration. Figure 5a shows a typical evolution of the profile of PSD, when electrons are scattered by whistler-mode hiss and chorus waves and are relatively slowly lost to the atmosphere (e.g., Thorne et al., 2005). For MeV energies, typical timescales of loss due to hiss waves are on a scale of 5–10 days (Lyons et al., 1972; Orlova et al., 2014, 2016), and for chorus waves, on a scale of 1 day (Orlova & Shprits, 2014). The loss rates show a relatively weak dependence on radial distance but a strong dependence on the geomagnetic activity (Thorne et al., 2005; Orlova et al., 2014; Orlova & Shprits, 2014). At multi-MeV, diffusion by hiss becomes slower and timescales may reach weeks or months (Shprits et al., 2013). In the absence of local acceleration, that produces growing peaks in PSD, the radial profiles should be monotonic, as radial diffusion timescales are likely to be shorter than that of very low frequency (VLF) wave scattering, and even an L-dependent loss cannot produce local dips, as the radial diffusion will smooth out the PSD.

Moreover, the VLF-wave-induced loss rates usually show little radial dependence compared to the radial dependence of radial diffusion (Thorne et al., 2005), which would not allow chorus or hiss waves to produce prominent localized dips in PSD radial profiles. The second scenario, Figure 5b, illustrates the loss due to the outward radial diffusion, driven by the loss to the magnetopause (Shprits, Thorne, Friedel, et al., 2006). In this case, profiles of PSD show decreasing peaks, which should not be confused with the buildup of peaks due to local acceleration. In this scenario, negative gradients in PSD profiles are formed as the outer boundary decreases (Selesnick & Blake, 2000). The third scenario (Figure 5c) shows a tell-tale signature of fast localized loss that can be produced by EMIC waves, which can result in strong diffusion (Kennel, 1969) and provide a loss on time scales shorter than an hour (e.g., W. Li et al., 2007; Summers & Thorne, 2003; Ukhorskiy et al., 2010).

Consistent with the picture revealed by the modeling discussed above, radial profiles of PSD at MeV energies (Figure 6a) are monotonic, indicating the absence of EMIC wave-driven loss. Contrary to this, the profiles at multi-MeV in Figure 6b clearly show deepening minima in PSD radial profiles during the September 2012 storm described (see Figures 3 and 4) above. Only localized and very fast loss can produce fast deepening minima, as slow loss would be smoothed out by the radial diffusion.

The deep minimum is formed at the same time as the outer boundary increases, demonstrating that the outward radial diffusion cannot produce the depletion seen below $L = 4$ and can only operate above $L \sim 4.7$ where gradients are negative, and radial diffusion transports particles outwards.

Additional validation (Figure 7) of this picture came from the comparison of multi-MeV profiles of PSD derived using different magnetic field models, in this case, T04s (Tsyganenko & Sitnov, 2005) and TS07D (Tsyganenko & Sitnov, 2007). The comparison of the radial profiles shows that the presence of dips in PSD is independent of the assumed magnetic field model and that errors associated with inaccuracy of models are much smaller than the observed dips in PSD.

While in general, it is difficult to isolate the loss due to EMIC waves and the loss due to the outward radial diffusion driven by the loss to the magnetopause, selected events such as September 2012 present a great opportunity to separately identify different processes. Another interesting storm occurred on January 17, 2013. During this event, the pre-existing MeV and multi-MeV belts were spatially separated. The multi-MeV belt was produced by a storm that occurred in October 2012, 101 days before the 17 January 2013 storm. During that time, electrons

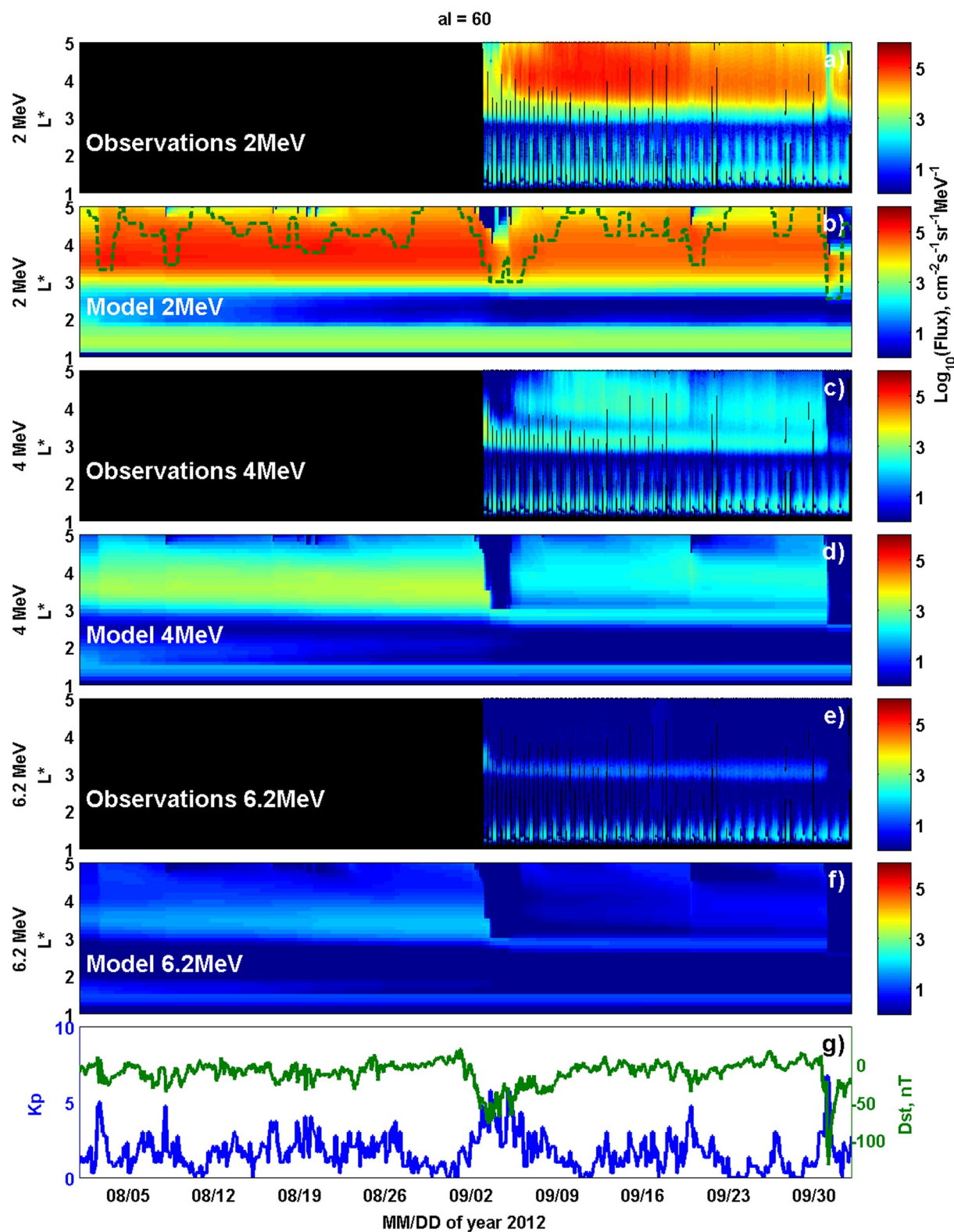


Figure 4. Comparison of simulations with the VERB code, including EMIC waves with observations. (b, d, f) VERB simulations including EMIC wave scattering (a, c, e) observations from the Relativistic Electron Proton Telescope (REPT) instrument on Van Allen Probes for kinetic energies of 2, 4, and 6.2 MeV. Panels (a)–(f) show omni-directional electron fluxes as a function of time and L^* . The bottom panels show K_p and Dst indices. The plasmapause is shown as a green line and is modeled according to Carpenter and Anderson (1992) in panel (b) (Adopted from Shprits et al., 2013).

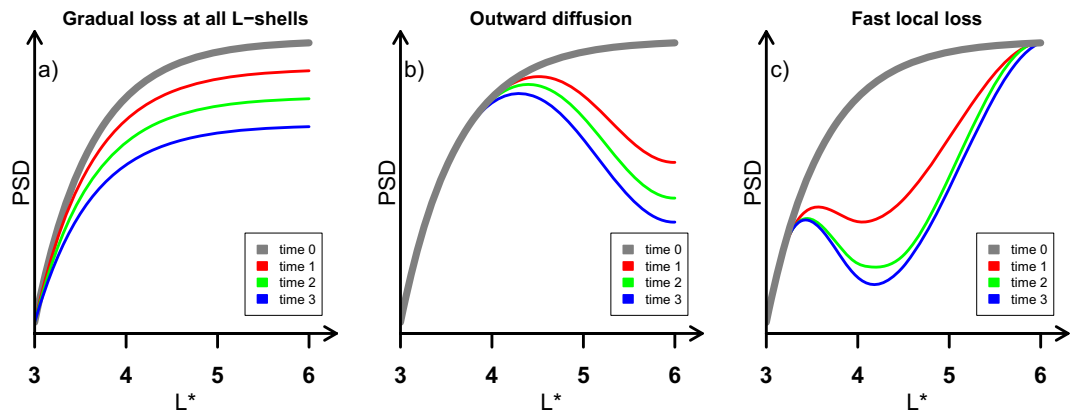


Figure 5. Illustration of the tell-tale signatures in the evolution of the PSD profiles illustrating three types of different loss mechanisms. (a) Gradual loss by hiss or chorus VLF waves; (b) sudden loss to the magnetopause which drives the outward diffusion; and (c) rapid localized loss that can be provided by EMIC waves that are often confined to a small region in space (Reproduced from Shprits et al., 2017).

were able to diffuse inwards down to $L = 2\text{--}4.5$. The MeV belt was located at higher radial distances above $L = 4.5$. For this event, the magnetopause and the calculated last closed drift shell did not move into geosynchronous orbit, allowing for the clear separation of the effects of EMIC waves and outward radial diffusion, driven by the loss at higher L -shells. Moreover, scattering by hiss and chorus waves at these energies is weak and can not produce the observed rapid loss.

During the January 17 storm (K_p only reaching 4, Figures 8a and 8b), the flux of relativistic electrons at ~ 1.02 MeV is enhanced (Figure 8c), likely due to the combination of inward radial diffusion and local acceleration moving

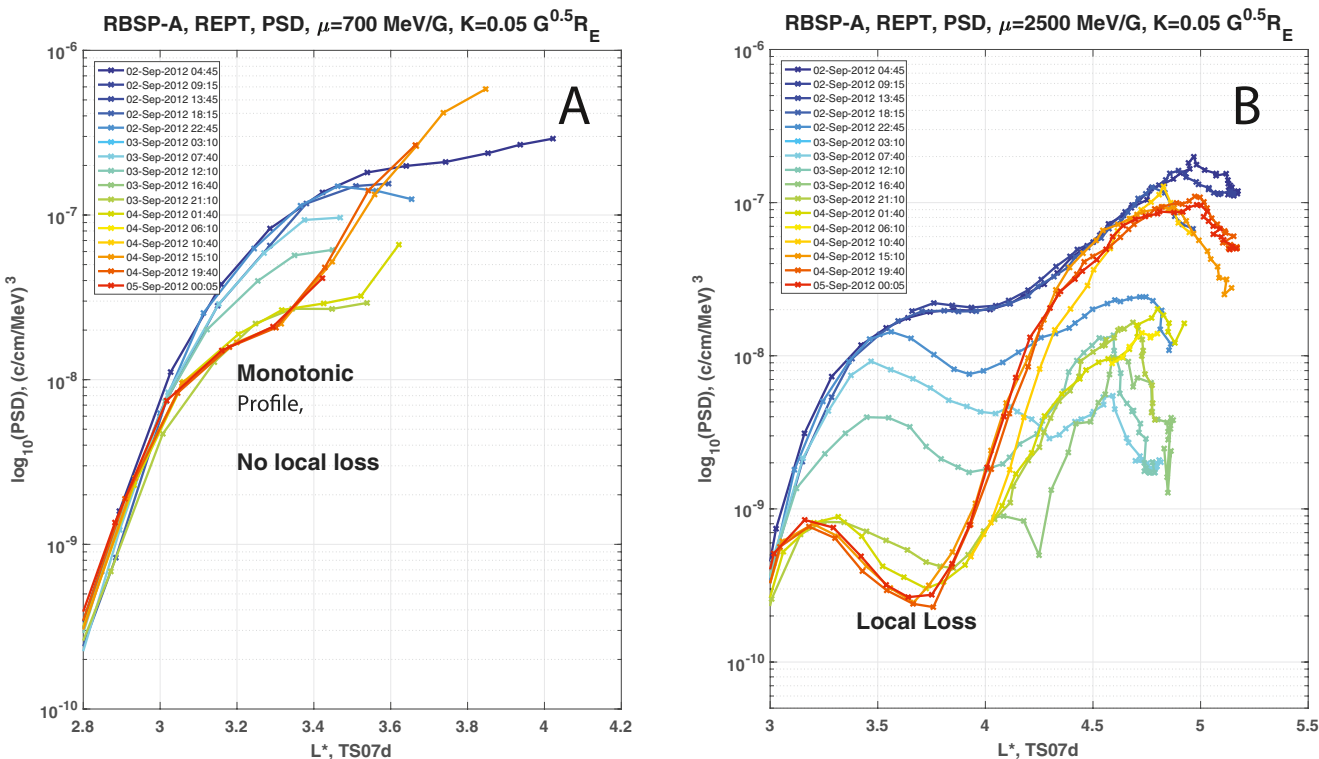


Figure 6. Radial profiles of PSD are given for different values of the first invariant. (left) Profiles of PSD obtained with TS07D model and (a) for $\mu = 700$ MeV/G, corresponding to MeV energies in the heart of the belt and, (right) (b) $\mu = 2500$ MeV/G, $K = 0.05 G^{0.5} R_E$, using TS07D model (Shprits et al., 2018).

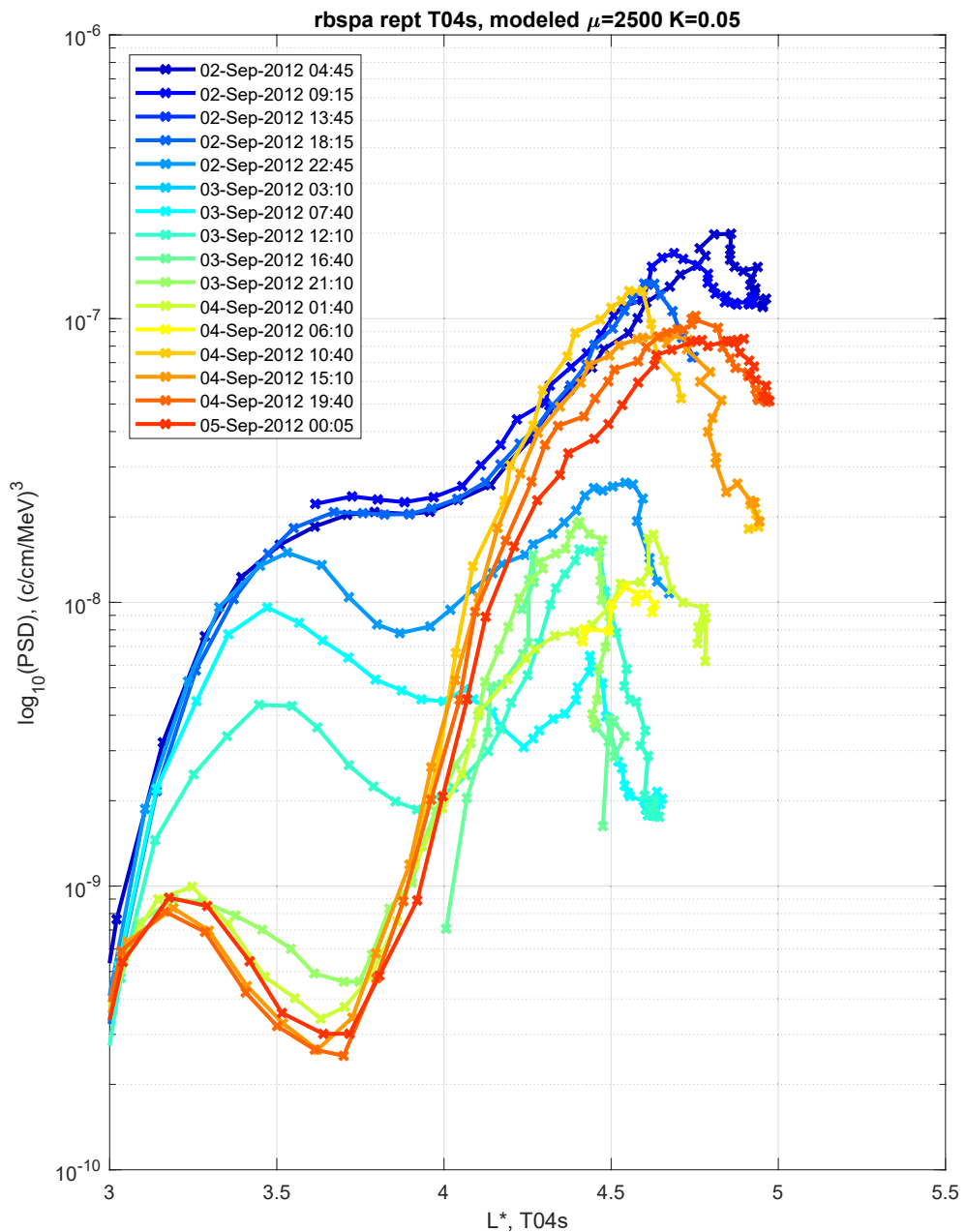


Figure 7. Profiles of PSD using different magnetic field models. (left, a) Profiles of PSD obtained with T04S (Tsyganenko & Sitnov, 2005) model and for $\mu = 2500$ MeV/G, $K = 0.05$ G $^{0.5}R_e$. (right, b). Similar to (a), but using the TS07D model (Shprits et al., 2018; Tsyganenko & Sitnov, 2007).

the inner edge of the outer belt closer to the Earth (Figure 8c). The short-lived dropout of the relativistic flux is associated with the reversible changes described in the supplementary material of Shprits et al. (2016). The adiabaticity of this dropout is confirmed through demonstrating that ions and electrons show the same dropout and recover to pre-storm values at the same time that Dst recovers (for more details, see Supplementary figure 1 and Supplementary Note 1 of Shprits et al. [2016]).

Unlike relativistic electrons, electrons with energies of 4.2 MeV (Figure 8d) show an irreversible decrease in flux. This loss is clearly not to the magnetopause, as the magnetopause for this event was compressed down to $7.1 R_E$, according to an empirical model <https://paperpile.com/c/D3f9TV/SqrU> of Shue et al. (1997) (see also Supplementary Note 2 and Supplementary figures 2 and 3 of Shprits et al., 2016). MeV electrons are enhanced as

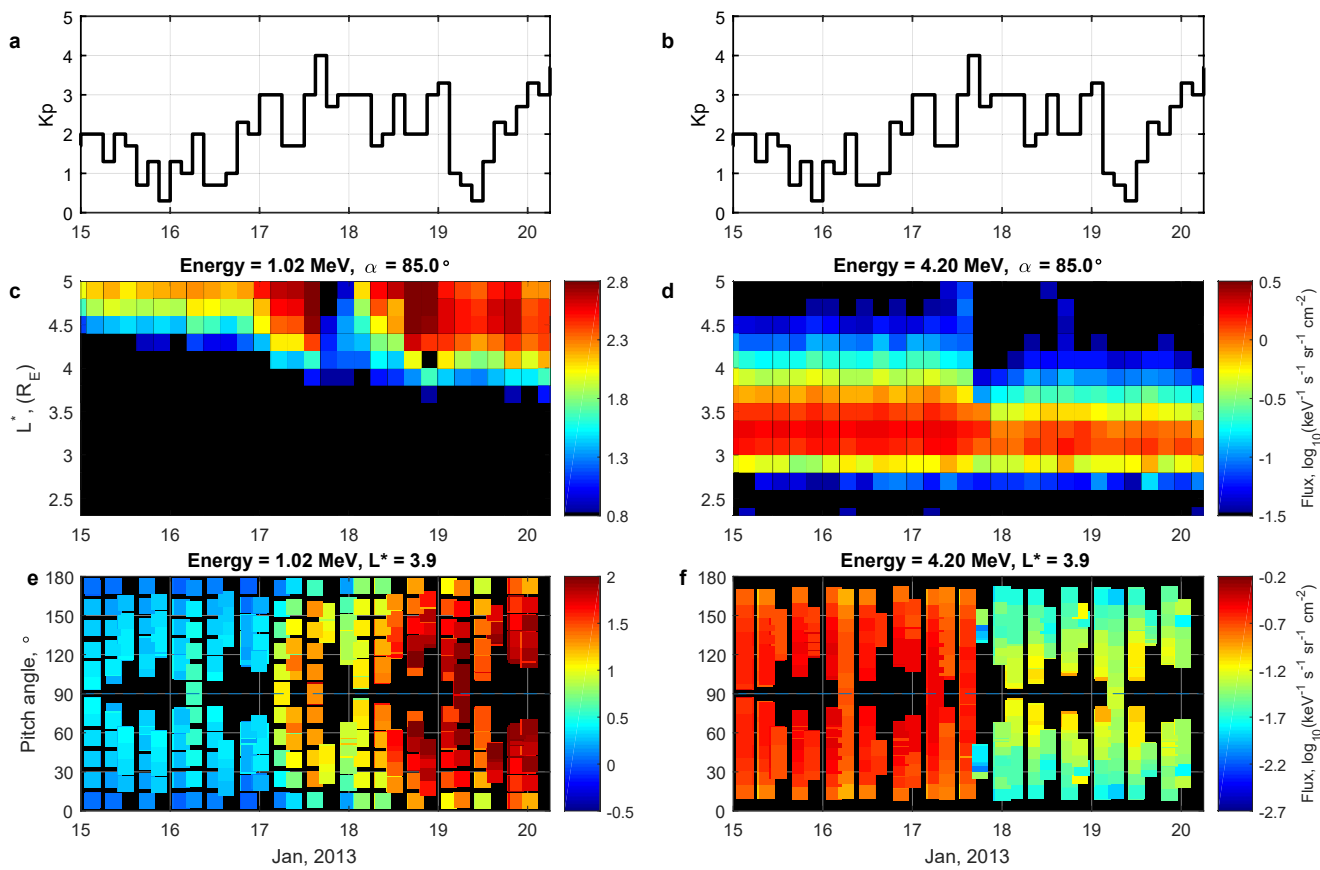


Figure 8. Van Allen Probes observations of electron fluxes and pitch angle distributions observed during the January 17, 2013 storm. (a) and (b) Evolution of the Kp index. (c) and (d) Observations of electron flux at 85° equatorial pitch angle as a function of L^* and time on MAGnetic Electron Ion Spectrometer (MagEIS) (c) $E = 1.02$ MeV and on REPT (d) $E = 4.20$ MeV. (e) and (f) Evolution of the pitch angle distribution for the same energies (Adopted from Shprits et al., 2016).

a result of this storm, while the multi-MeV outer electron belt is depleted down to below $4.5 R_E$. Such differences in the evolution of fluxes between relativistic and ultra-relativistic electrons for this storm can only be explained by the presence of loss due to EMIC waves, similar to the event in September 2012 described above. EMIC waves affect only electrons above a certain minimum threshold energy, which explains why the multi-MeV electrons are scattered, while electrons at MeV are unaffected. Further evidence for the EMIC-induced loss comes from the observation of pitch angle distributions of electrons (Figures 8e and 8f). During interactions with EMIC waves, only electrons at small pitch angles, for which the Doppler-shifting is strongest, are capable of resonating with EMIC waves. Such fast scattering by EMIC waves produces characteristic bite-outs near 0° and 180° . Higher pitch angles can also be lost, as scattering by EMIC waves is assisted by VLF waves (Drozdov et al., 2020; W. Li et al., 2007; Shprits et al., 2009, 2016), but the characteristic shape, with very few particles near the loss cone and where EMIC waves are most efficient, will remain. The 4.2 MeV electron distribution shows clear bite-outs near the loss cone, with sharp gradients around 50° and 130° , indicative of fast scattering by EMIC waves. In contrast, the pitch angle distribution of relativistic electrons is rather wide and smooth (Figure 8e).

Measurements from ground stations in Finland showed that EMIC waves were present on January 17, 2013, between approximately 15 and 18 UT, with a peak intensity at Oulu station near $L = 4\text{--}4.5$, exactly in the same place and at the same time as the dropout in fluxes of ultra-relativistic electrons (Figure 8d) and the appearance of the bite outs in the pitch angle distributions (Figure 8f; see also Supplementary Note 4 of Shprits et al. [2016]).

Simulations of relativistic electron radiation belt dynamics, including radial transport and local acceleration and loss due to whistler-mode waves (Figure 9a), can well reproduce the dynamics of 1.02 MeV electrons (Figure 4e). Simulation of 4.2 MeV electrons using VERB-3D code without EMIC waves shows an increase in fluxes (Figure 9b), while observations clearly show the dropout (see Figure 9f for comparison). The introduction of

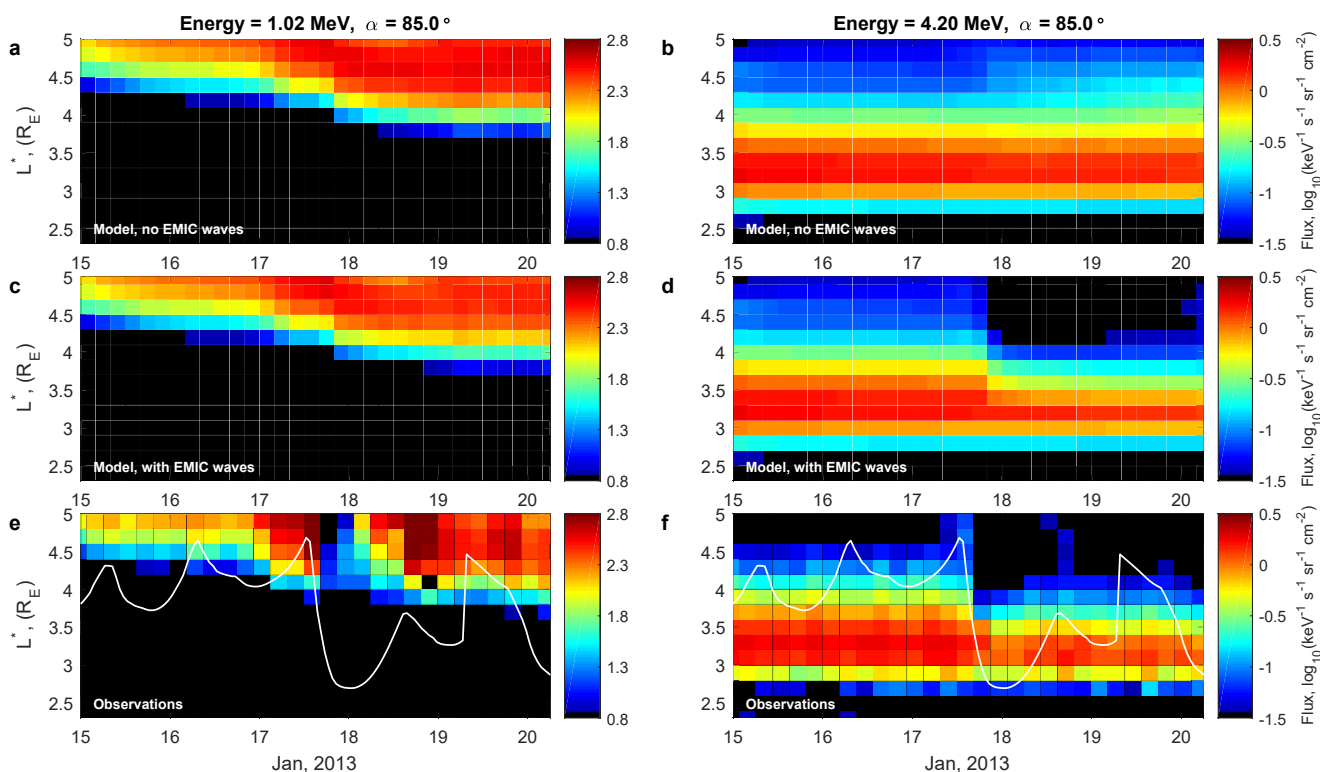


Figure 9. Comparisons of the VERB-3D model results and observations of the evolution of fluxes of electrons at 85° equatorial pitch angle starting on January 15, 2013. The VERB-3D simulations without EMIC waves are shown for 1.02 and 4.2 MeV on panels (a) and (b), respectively. Simulations including EMIC waves are shown on panel (c) for 1.02 MeV and (d) for 4.2 MeV electrons. Van Allen Probes' observations are shown on panels (e) and (f) for the same set of energies. The white line indicates the plasmapause location (Adopted from Shprits et al., 2016).

EMIC waves into the VERB-3D simulation on January 17 for 3 hr between 15 and 18 UT, does not substantially change the dynamics of the relativistic electrons (Figure 9c), but produces a dropout in fluxes at ultra-relativistic energies (Figure 9d) consistent with observations (Figure 9f). Modeled pitch angle distributions in Figure 10 provide additional evidence for scattering by EMIC waves. Observations of the bite-outs for small pitch angles at the beginning of the storm (Figure 10f) are well reproduced by the VERB-3D simulations, which present clear tell-tale signatures of EMIC wave scattering and are very similar to the modeled evolution of pitch angle distributions, including EMIC wave effects (Figure 10d).

The scale of the dropout at $L = 3.9 R_E$ and the narrow shape of the pitch angle distribution observed on the Van Allen Probes (Figure 10d) are well reproduced by the simulations with EMIC waves (Figure 10f). The modeled pitch angle distributions at energies of 0.46 and 3.4 MeV also agreed with observations and were presented in Supplementary figure 6 of Shprits et al. (2016).

While EMIC waves cannot directly affect near-equatorially mirroring electrons, they can develop the gradients in PSD (Figure 10f), facilitating the transport from high pitch angles induced by hiss or chorus waves. Detailed sensitivity simulations of combined scattering by VLF and EMIC waves have been done by Shprits et al. (2009), and 3D simulations of such combined scattering has been recently performed and discussed in detail by Drodzov et al. (2020).

Similar to the analysis of dips in PSD performed for the September 2012 storm, Figure 11 shows PSD as a function of L^* and time during the January 17, 2013 storms. For the PSD inferred for $\mu = 700$ MeV/G, corresponding to MeV energies, the radial profiles are monotonic, gradually increasing with increasing radial distance. There is an increase in the PSD above $L^* = 4.5$ due to the local acceleration and inward radial diffusion. At $\mu = 3,500$ MeV/G and $K = 0.1 G^{1/2} R_E$, which corresponds to the kinetic energy of 4.63 MeV at $L = 4$ in a dipole field, there is a pronounced formation of the deepening local minimum during the times when the PSD at $L^* = 5.5$ is increasing. The minimum becomes more pronounced for the increasing first invariant. Supplementary figures 3 and 4 of

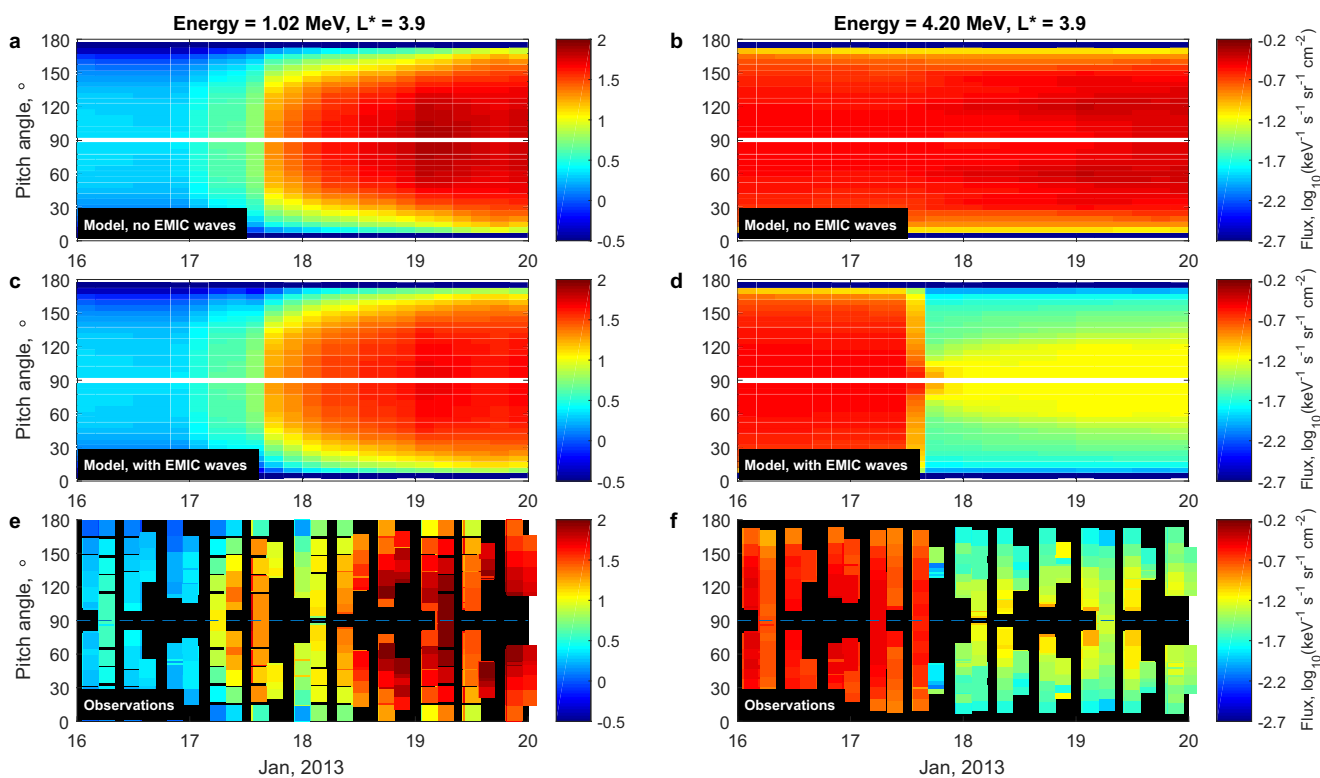


Figure 10. Comparisons of the VERB-3D model pitch angle distributions and the evolution of pitch angle distributions at $L = 3.9$ starting on January 15, 2013. The VERB-3D simulations without EMIC waves are shown for 1.02 and 4.2 MeV on panels (a) and (b), respectively. Simulations, including EMIC waves, are shown on panel (c) for 1.02 MeV and (d) for 4.2 MeV electrons. Van Allen Probes' observations of pitch angle distributions are shown on panels (e) and (f) for the same set of energies (Adopted from Shprits et al., 2016).

Shprits et al. (2017) showed similar local minima when PSD was calculated with two magnetic field models (T89 [Tsyganenko, 1989], T04S [Tsyganenko & Sitnov, 2005]), demonstrating that the minima are not an artifact associated with inaccuracies of the magnetic field model.

Figure 12 illustrates how the dips in profiles are formed. There is no indication of dips in PSD at the lower energies of 300 and 500 MeV/G. At 1,500 MeV/G, a weak minimum begins to form. At $L^* = 4$, this μ and K pair corresponds to an energy of 2.58 MeV in the dipole magnetic field model. The minimum becomes more pronounced at 3.46 and 4.17 MeV, as shown in Figures 12c and 12d.

Figure 13 provides a longer-term evolution of the radial profile of PSD at $\mu = 3,500$ MeV/G, for the entire month of January 2013. Starting on January 17, 2013, observations show that a pronounced minimum in PSD formed between January 17 and 18, at around $L^* = 4$. This minimum persists for over 2 weeks. While the pronounced minimum is deepening, there is an increase in PSD at higher L -shells of approximately 4.5. The decrease in PSD cannot be produced by the outward radial diffusion, as PSD in the outer region increases, and the gradients in PSD are positive. Such a localized and fast loss cannot be due to hiss or chorus waves, as the time scales associated with these waves are very long for ultra-relativistic energies. The minimum in PSD is further deepened during the March 1, 2013 storm. The minimum moves to lower L -shells, while PSD above $L^* = 4$ increases.

In a recent study, Blum et al. (2020) analyzed in detail an EMIC wave event that occurred on July 7, 2013. For this event, the waves had a narrow radial extent but persisted for over 10 hr and spanned a local time region of ~ 12 hr. The radial profiles once again showing local dips in PSD, confirmed the loss of ultra-relativistic electrons during this event, while relativistic electrons remained unaffected by waves.

The observations of dips in PSD profiles are consistent with conclusions made from the modeling studies of Shprits et al. (2016). It is clear that at least for January 17, 2013, and September 2012 events, the EMIC wave scattering only affects electrons above certain threshold energy of \sim a few MeV and does not seem to significantly

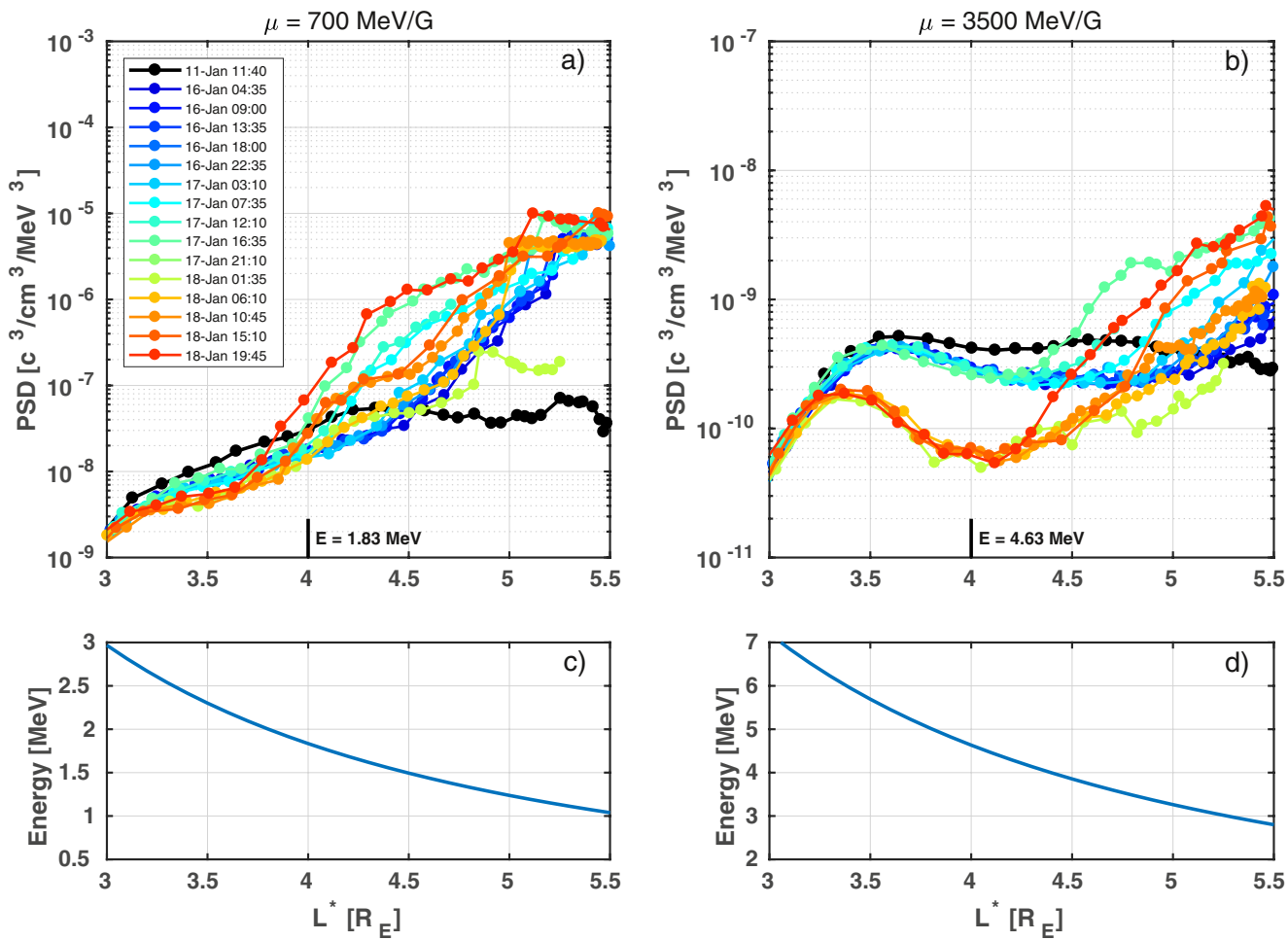


Figure 11. Radial profiles of PSD for (a) relativistic ($\mu = 700 \text{ MeV/G}$) and (b) ultra-relativistic ($\mu = 3,500 \text{ MeV/G}$) electrons for $K = 0.1 \text{ G}^{1/2} R_E$, measured by RBSP-B. The black line shows undisturbed pre-storm conditions, and colors-coded is the time that corresponds to the end of the inbound and outbound orbital passes. Bottom panels (c) and (d) show energy for this value of the first invariant inferred using the dipole field. Profiles of PSD were calculated with the TS07D model (Tsyganenko & Sitnov, 2007). (Adopted from Shprits et al., 2017).

affect MeV electrons. The minima in PSD help to identify and visualize the exact location of the scattering and its effectiveness.

Understanding of the loss by EMIC waves can also be obtained from simultaneous observations of waves on the ground and narrowing distributions in pitch-angle space. In Usanova et al. (2014), the presence of EMIC waves was inferred from CARISMA chain ground magnetometers by visual inspection. To objectively quantify the effect of EMIC waves on pitch-angle distributions and to be able to compare the distributions at different energies, Usanova et al. (2014) normalized the pitch angle distributions by the flux of equatorially mirroring electrons so that, regardless of energy, the value of the normalized distribution near 90° is 1. The observations showed that, in general, the presence of waves coincided with the narrowing of the pitch angle distributions. Aseev et al. (2017) extended the analysis of Usanova et al. (2014) and derived profiles of PSD, which revealed dips in PSD indicative of localized loss (shown in Figure 14), as discussed above and illustrated in Figures 6, 7, 11 and 12. The analysis of observations from September 9 until November 29, 2012 by Aseev et al. (2017), showed that the presence of EMIC waves on the ground not only coincided with the narrowing of the pitch angle distributions, but also with the presence of dips in PSD as discussed above, providing a very convincing picture of scattering by EMIC waves. Typical tell-tale signatures of EMIC scattering in the pitch angle distributions, dips in radial profiles of PSD, and observations of waves on the ground (Aseev et al., 2017) all pointed to scattering of multi-MeV by EMIC waves. In addition, statistical study of pitch angle distributions by Drozdov et al. (2019)

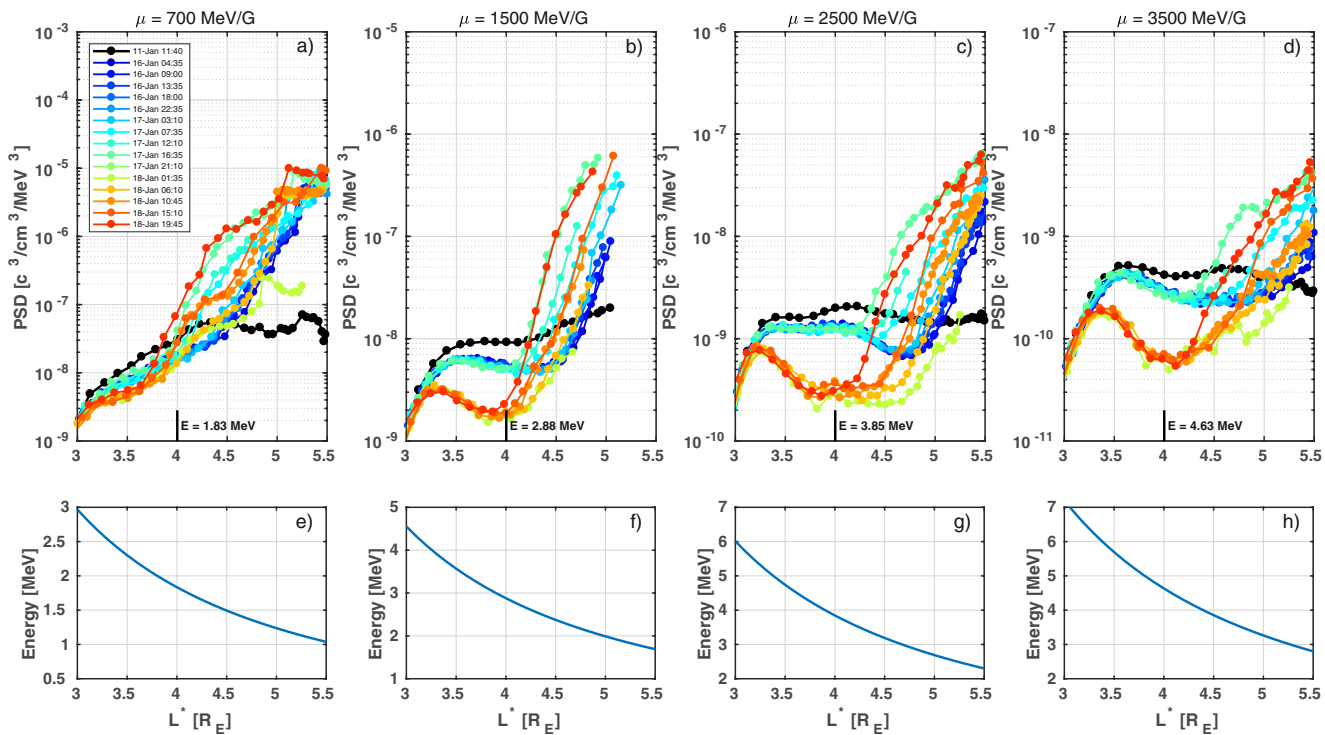


Figure 12. Similar to Figure 11, except for a number of values of the first invariant from 300 to 3,500 MeV/G (Adopted from Shprits et al., 2017).

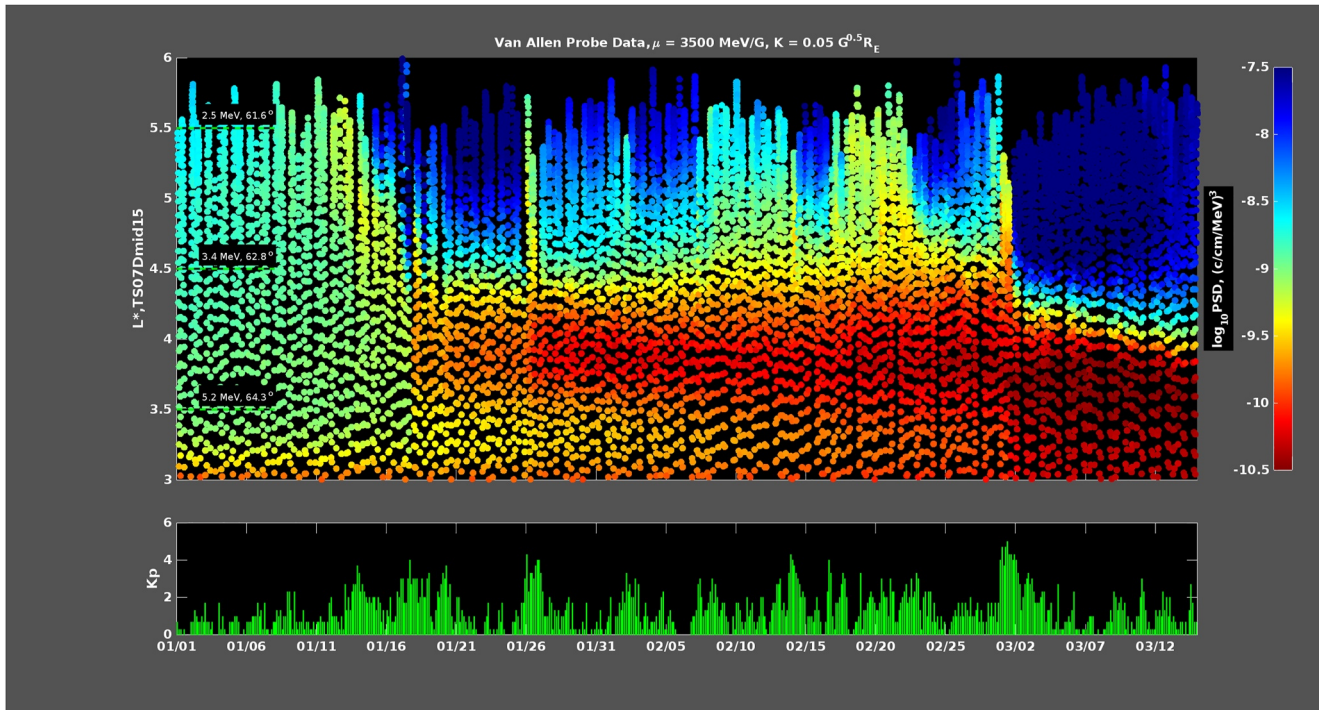


Figure 13. Evolution of the PSD from January 1, 2013, until March 1, 2013. PSD is given for $\mu = 3,500 \text{ MeV/G}$ and $K = 0.05 \text{ G}^{1/2} \cdot R_E$ as a function of tie and L^* . The bottom panel shows the evolution of the Kp index (Adopted from Shprits et al., 2017).

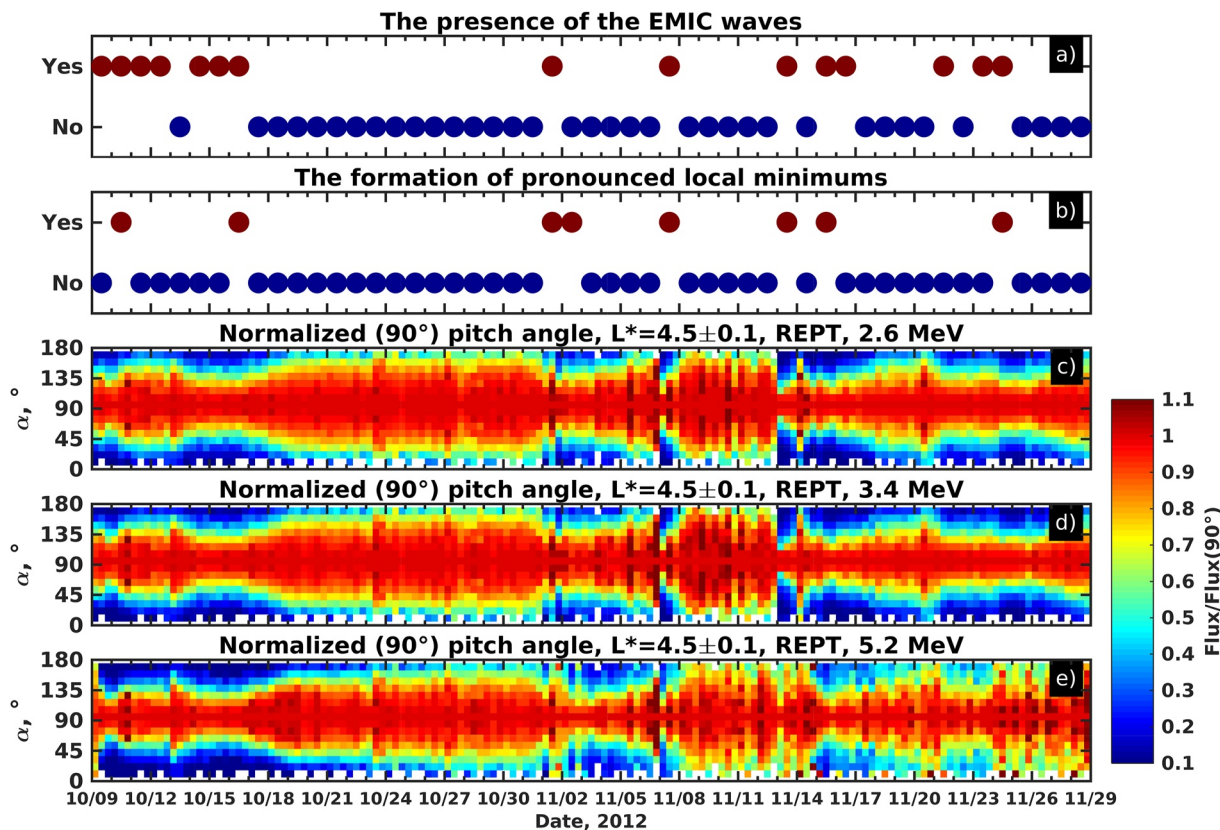


Figure 14. (a)–(e) The presence of EMIC waves observed by CARISMA stations at $L = 4\text{--}4.5$ between October 9 and 29 November 2012. (b) "Yes" or "No" flag showing the formation of a new dip in phase space density. (c)–(d) Normalized to 90° pitch angle distributions measured by REPT on board Van Allen Probes in 2.6, 3.4, and 5.2 MeV energy channels as a function of time at $L^* \sim 4.5$, computed using the TS07D magnetic field model (Tsyganenko & Sitnov, 2007). [Adopted from Aseev et al., 2017].

showed that the most of the depletion of multi-MeV electrons at $L^* < 5.2$ during storms are in agreement with the EMIC waves scattering.

EMIC waves may be observed in three distinct bands Hydrogen, Helium, and Oxygen. Many of the previous in-situ studies of waves concentrated on the He band as the frequency of occurrence of the EMIC waves is the highest in this band. However, Hydrogen band waves may also play an important role, and resonance energies for this band may be lower for the Hydrogen band than for the Helium band (Cao et al., 2017). Qin et al. (2019) observed an interesting event where waves were observed in the hydrogen band. The comparison of time-shifted flux profiles on RBSP-A with profiles on RBSP-B helped reveal a rapid loss process. RBSP-A measurements are shifted by 64 min to match the location of RBSP-B. Most interesting for these events is that, below $L = 4$, the difference between the observed fluxes is only seen at energies of 2.6 MeV and above. As shown in Figure 15, the fast dropout that occurs on timescales of less than an hour becomes more pronounced, and the loss is seen closer to the Earth as the energy increases.

Several studies (Thorne & Kennel, 1971; Summers et al., 1998; Albert, 2003; W. Li et al., 2007; Ukhorsky et al., 2010) showed that if the frequency of waves is sufficiently close to the local gyro-frequency, EMIC waves can resonate with electrons at energies below 1 MeV, while the observations discussed above demonstrate that predominantly multi-MeV are scattered by EMIC waves. To resolve this seemingly apparent disagreement between models and theory, Cao et al. (2017) considered the hot plasma dispersion relation and solved for both frequency and linear growth rates. They estimated the Minimum Resonance Energies (MRE) by considering the marginal frequency when the growth rate is zero. They considered the hydrogen and helium bands where the waves are usually observed and performed sensitivity calculations for the typical parameters controlling the resonance energies. The MRE was calculated for zero-degree equatorial pitch angles, which provided a lower bound for the estimate of the energies that the EMIC waves can effectively scatter. This study used the values

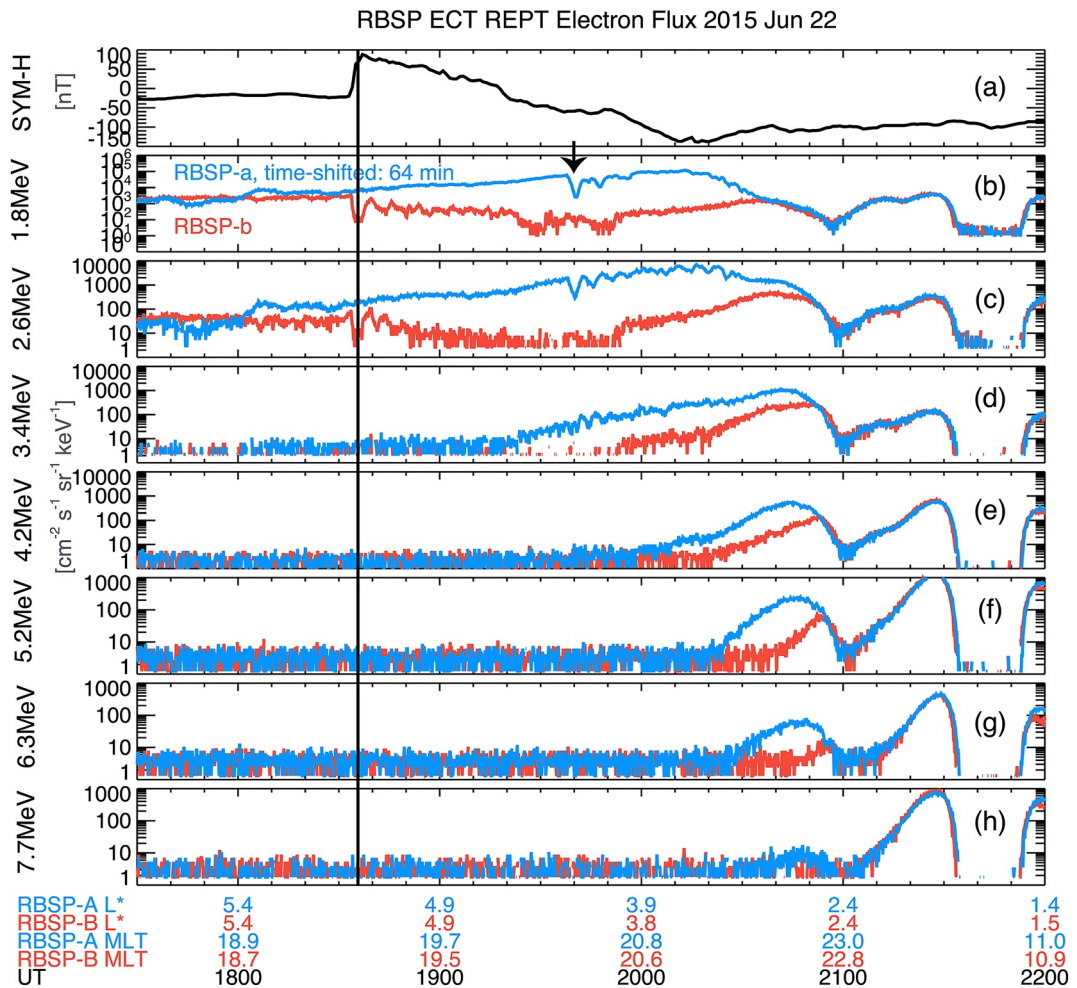


Figure 15. Overview of the electron profiles from 1730 to 2200 UT. (a) SYM-H geomagnetic index. The shock arrived at 1836 UT. (b)–(h) The omni-directional differential flux at energies of 1.8-, 2.6-, 3.4-, 4.2-, 5.2-, 6.3-, and 7.7-MeV electrons, measured by RBSP-A (blue) and RBSP-B (red) spacecraft. MLT and L^* are shown at the bottom of the figure on the X-axis. The vertical solid line indicates the shock arrival at 18:36 UT. The time corresponds to Van Allen Probe B, and Van Allen Probe A is shifted by 64 min. The black arrow indicates shock arrival time at Van Allen Probe (a) [Adopted from Qin et al., 2019].

of the plasma number density obtained from the Neural-network-based Upper-hybrid Resonance Determination (NURD) machine learning algorithm (Zhelavskaya et al., 2016), utilizing Electric and Magnetic Field Instrument Suite and Integrated Science (EMFISIS) observations, Kletzing et al. (2013) data and also compared the NURD densities with the statistical model of Sheeley et al. (2001). They first performed sensitivity experiments for the calculated MRE to the assumed hot plasma anisotropy for various density values (Figure 16). To take into account the ion composition (Figure 1), they inferred the MRE for four realistic models of the ion composition listed in Table 1. The multiple sensitivity calculations showed that only for very high density, extremely high anisotropy, and preferential plasma composition, it was possible to lower the MRE below 1 MeV. Most of the calculations showed that the MRE for both the helium and hydrogen bands lies above 2 MeV, which is consistent with observations discussed above in this section. Calculations of MRE in hot plasma provide a theoretical explanation of why the resonance usually lies above ~ 2 MeV.

While for a particular set of conditions it may be possible for waves to be in resonance with ~ 1 MeV electrons and such scattering can be seen in idealized models (for example, Denton et al., 2019), observations and theory both indicate that such interactions are not as frequent and likely as at multi-MeV energies. It still remains unclear if under certain conditions, EMIC wave scattering may potentially contribute to the scattering of 1 MeV or even sub-MeV electrons.

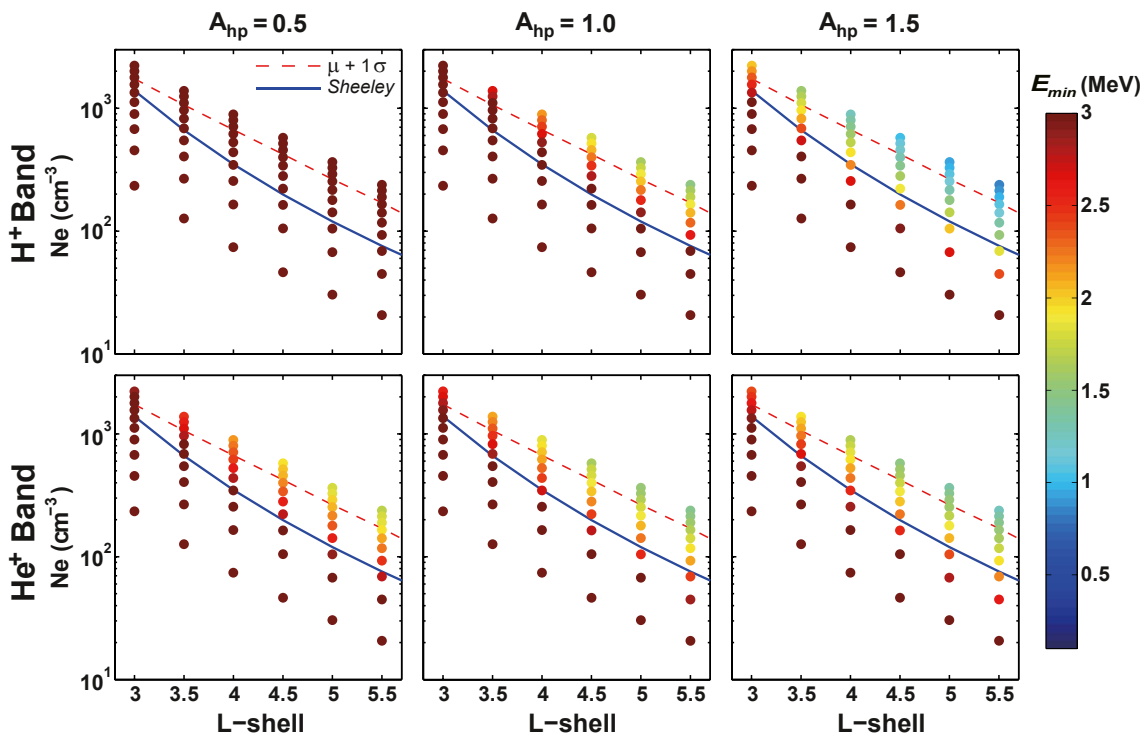


Figure 16. Sensitivity of electron minimum resonance energy (MRE) to the anisotropy of hot H⁺ protons. Electron MRE is presented as a function of L-shell and electron number density for various hot H⁺ temperature anisotropies ($A_{hp} = 0.5, 1.0, \text{ and } 1.5$) for helium and hydrogen EMIC wave bands. Red dashed lines show the electron density one standard deviation above the mean value of NURD measurements. Blue solid lines denote electron densities from Sheeley et al. (2001) an empirical density model, which is frequently used as the statistical average value for density [Adopted from Cao et al., 2017].

In a recent study L. Chen et al. (2019) analyzed the EMIC wave number and inferred the minimum resonance energy directly from these observations. While the method of inferring the wave number from just two spacecraft may have substantial uncertainty, it allows to directly infer the MRE without making additional assumptions on the wave dispersion relation. The results of this analysis showed that most of the MRE of the analyzed event were above 2 MeV, with the smallest MRE values reached only for the Hydrogen band. Further evidence for the selective scattering of electrons above multi MeV came from data assimilation studies. Cervantes et al. (2020) performed data assimilation with Van Allen Probes data, including and neglecting the scattering of EMIC waves in the VERB code. The innovation vector, measuring how much data corrects the model, was used to determine the importance of EMIC waves. In particular, they considered the difference in innovation between the data assimilative run with the code that included and neglects EMIC waves. The results indicated that in general, the outward radial diffusion produces the majority of the loss for radiation belt electrons. However, during the storm, the inward edge of the loss of multi-MeV can be dominated by EMIC waves.

The understanding of how EMIC waves drive the loss of ultra-relativistic radiation belt electrons has vastly improved in recent years. This is not only due to the availability of the Van Allen Probes measurements of particles for a wide range of energies and waves, but also due to the development of numerical models. 3D modeling, observations, theoretical calculation of MRE, data assimilation, and 3D sensitivity simulations show a consistent picture of multi-MeV electron scattering by EMIC waves during selected storms. Such a clear signature of EMIC wave scattering has not been observed for MeV electrons. Although questions still remain in regard to EMIC wave occurrence and MRE, careful analysis of PSD profiles along with the agreement of

Table 1
Models of Ion Composition Used for Figure 17 (Adopted From Cao et al., 2017)

Ratio	He+/H+	O+/H+
1	5%	10%
2	5%	50%
3	10%	10%
4	10%	50%

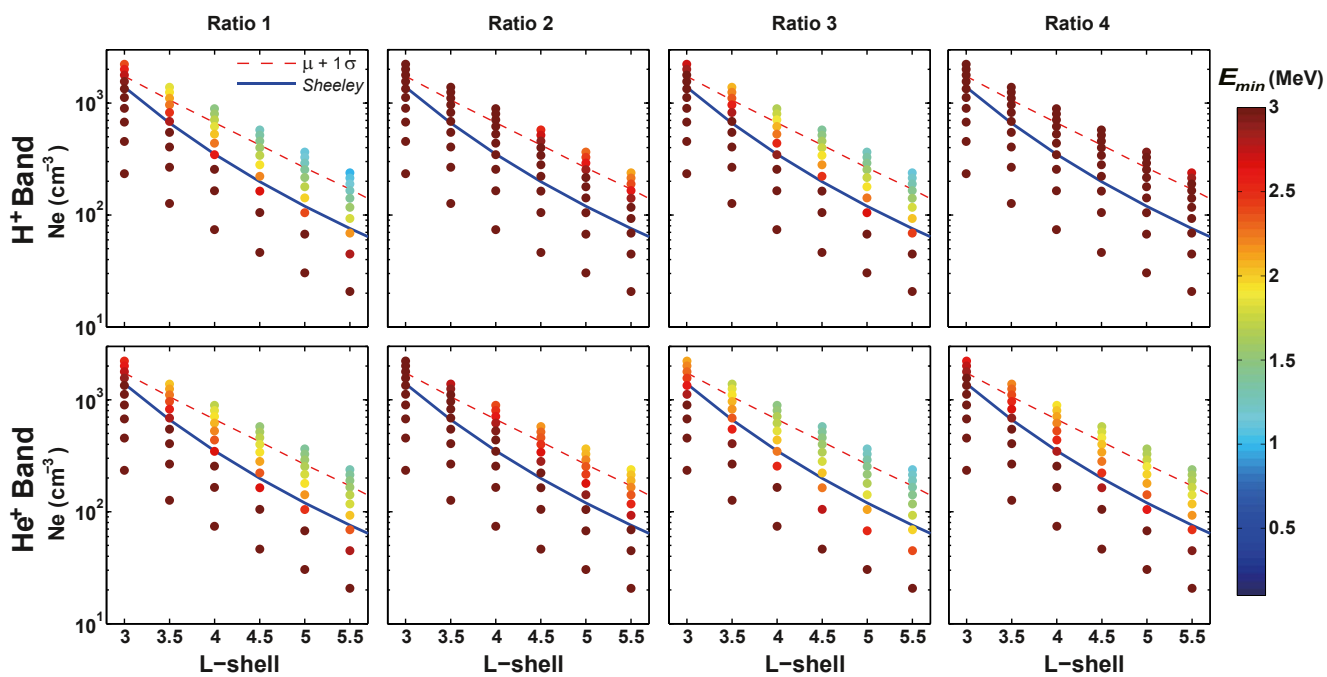


Figure 17. Sensitivity of electron MRE to the ion composition. Electron MRE is presented as a function of L-shell and electron density for different concentrations of H⁺, He⁺, and O⁺ ions corresponding to hydrogen and Helium band EMIC waves. Different models are presented in Table 1. The lines on the plot are the same as in Figure 16 [Adopted from Cao et al., 2017].

simulations and observations, have demonstrated the important role EMIC wave-particle interactions play for the dynamics of ultra-relativistic electrons.

3. Acceleration to Multi-MeV Energies

The broad coverage of the electron energies by the Van Allen Probes observations has allowed for the comparison of particle population dynamics at different energies. Figure 18 shows the dynamics of ring current electrons responsible for the generation of waves that can accelerate electrons and scatter them into the loss cone, along with relativistic and ultra-relativistic electrons. The flux of ring current electrons is highly variable. Changes in the strength of convection, and possibly localized electric fields, result in a very dynamic (localized in time and MLT) injection of particles that are then sampled by a spacecraft at a particular time and a single point in space. Such sparsity of measurements complicates the analysis and hinders the understanding of the physical processes responsible for the dynamics of these particles. Relativistic electrons show a much clearer and predictable pattern, demonstrating first depletion and then enhancements for most storms. In general, enhancements are stronger for stronger storms, as measured by K_p (see Borovsky and Shprits [2017] for the discussion of indices that can be used as a measure of activity). The dynamics of the ultra-relativistic electrons are clearly different from the relativistic electrons. Very sudden intensifications occur only for selected events and do not necessarily occur for all strong storms, as measured by K_p. Ultra-relativistic belts also tend to promptly disappear, driven by the loss to the magnetopause and the loss by EMIC waves in the heart of the belts, as discussed in Section 2. This section discusses the physics behind this acceleration, identifies mechanisms responsible for this acceleration, and spatial conditions in the magnetosphere when such acceleration to ultra-relativistic energies occurs.

Historically, radial diffusion was considered the dominant acceleration mechanism [for example, Falthammar, 1965; Schulz & Lanzerotti, 1974; Walt, 1994]. In this process particles diffusing into the region of a stronger magnetic field, while conserving the first and the second invariants, will gain energy. However, several studies have shown that the radial diffusion is not the only acceleration mechanism, and particles can also be heated locally by taking energy from the whistler-mode chorus waves (Y. Chen et al., 2007; Green & Kivelson, 2004; Horne et al., 2005; Iles et al., 2006; Reeves et al., 2013; Shprits, Thorne, Horne, et al., 2006; Thorne et al., 2013).

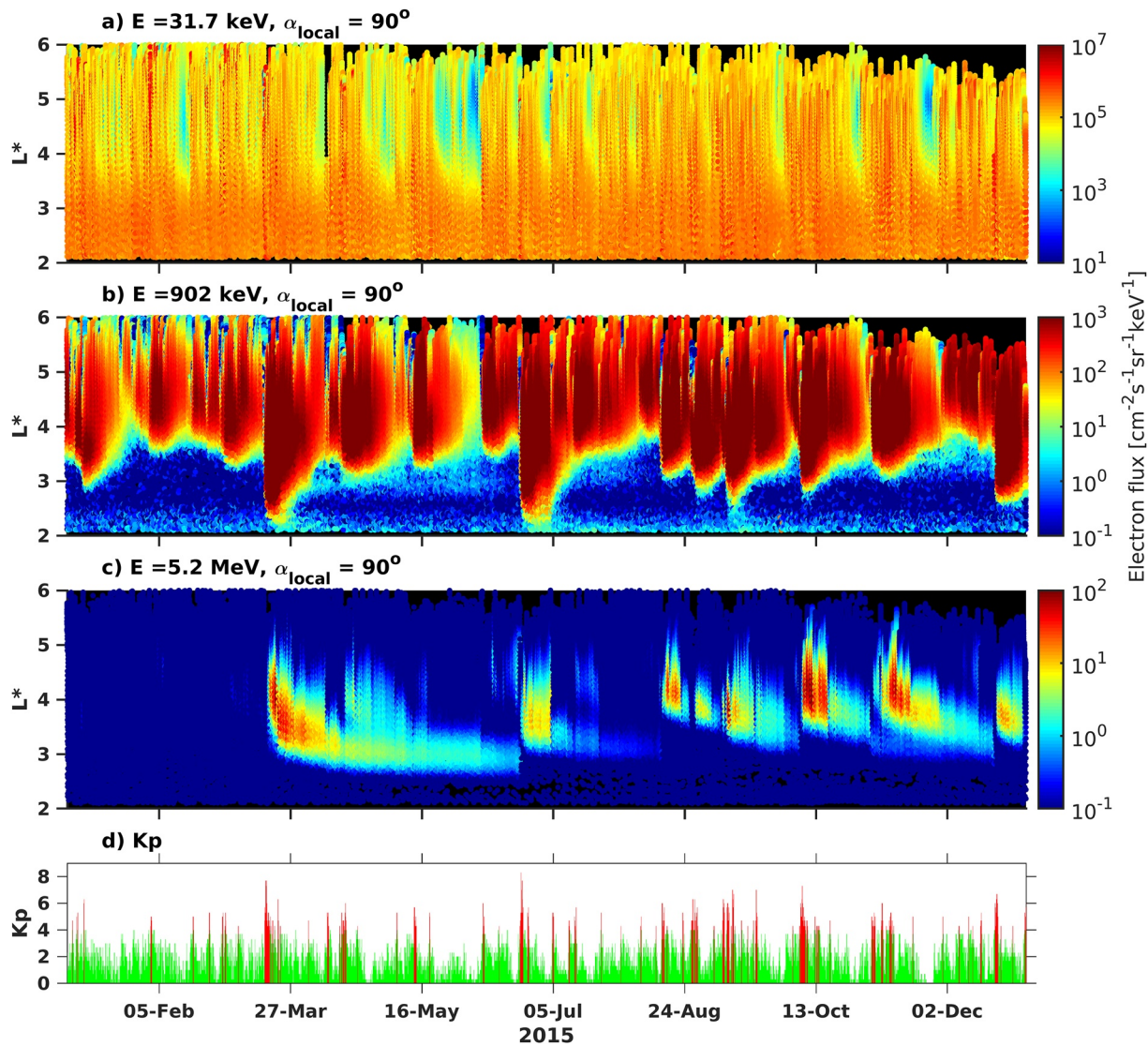


Figure 18. Comparisons of ring current relativistic and ultra-relativistic electron fluxes in 2015 from Van Allen Probes instruments MagEIS and REPT. (a–c) Correspond to energies of 3.7 keV, 902 keV, and 5.2 MeV, respectively. Panel (d) shows geomagnetic index K_p .

Identifying the presence of local acceleration is possible by looking at the radial profiles of the PSD and finding the time intervals for when local growing peaks are observed (Green & Kivelson, 2004).

Reeves et al. (2013) presented PSD profiles for relativistic radiation belt electrons. They observed growing peaks in the PSD for $\mu = 3,433 \text{ MeV/G}$ and $K = 0.11 R_E G^{1/2}$, which correspond to $\sim 3 \text{ MeV}$ at $L = 4.5$. In Figure 19, PSD for RBSP-A (squares) and RBSP-B (circles) is color-coded and labeled with the time at which each of the satellites crossed $L^* = 4.2$. The buildup of PSD near $L^* = 4.2$ is a clear, tell-tale signature of the local acceleration. If acceleration to these high energies was produced by the radial diffusion alone, the resulting profiles would be monotonic, with the largest value of PSD reached at the highest L-shell for which observations are available. Figure 19 clearly shows that for this event, this is not the case. The study concluded that for the 9 October 2012 storm, the observed profiles of PSD were consistent with the local acceleration and inconsistent with a predominantly radial diffusion model. The study showed that peaks at this value of the first invariant were observed for a number of different magnetic field models, indicating that the results of the study are independent of how the observations were converted to PSD.

Using a 2-D diffusion model at $L^* = 5$, Thorne et al. (2013) reproduced Van Allen Probes observations of the electron flux via local acceleration with chorus waves. Using a simple 2D code with relatively low plasma

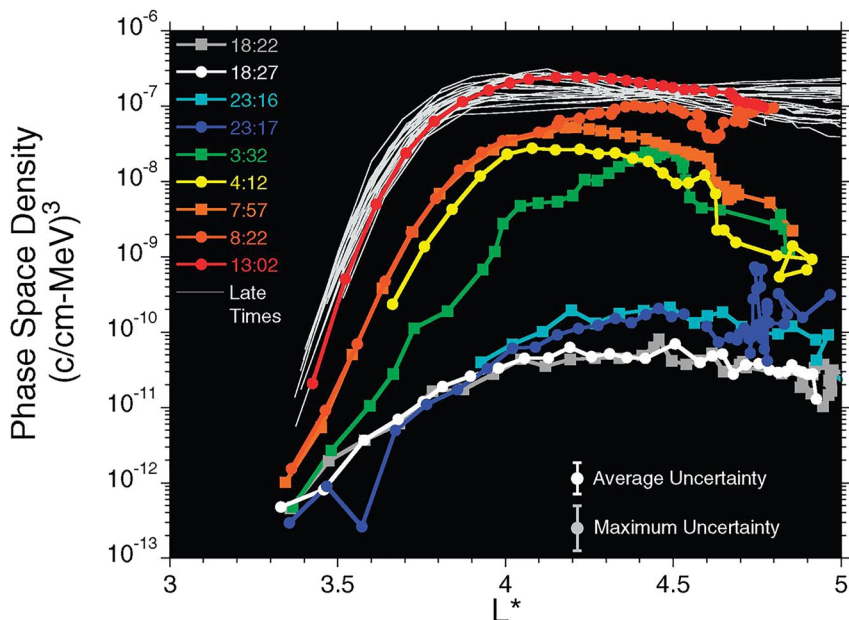


Figure 19. PSD profiles for relativistic radiation belt electrons measured by Relativistic Electron Proton Telescope (REPT) instrument on 8 and 9 October 2012 (Baker, Kanekal, Hoxie, Batiste, et al., 2013). Phase space density is in units of $(\text{c}/\text{cm}^{-3} \text{ MeV})^3$, where c is the speed of light [Adopted from Reeves et al., 2013].

density inferred from spacecraft observations, Thorne et al. (2013) demonstrated that electrons may be accelerated locally to 7 MeV. Since the simulations were only performed in 2D, the potential contribution of radial diffusion to the acceleration of ultra-relativistic electrons remained unclear. While the study did not explicitly discuss the unusual density values that were used for simulations derived from The Electric and Magnetic Field Instrument Suite(EMFISIS) spectrograms, the values were very low and below statistical values. It remained unclear however, how common it is for such low values to occur and if this dropout in density was global in MLT and L. It also remained unclear if it is reasonable to assume that such low density can persist for a sufficiently long time, which would be required for the substantial local acceleration to occur.

Recent studies (Boyed et al., 2016; Jaynes et al., 2015; Katsavriis et al., 2019; Zhao et al., 2019) have suggested that a multistep acceleration process in which electrons are first accelerated to relativistic energies locally by chorus waves and then diffuse inwards and gain further energy due to the radial diffusion, was responsible for the acceleration to such high energies. If this multistep process was indeed responsible for the acceleration to ultra-relativistic energies, then the growing PSD peaks would first be seen at large radial distances and subsequently broaden due to radial diffusion.

In a recent study, Allison and Shprits (2020) focused on the October 2012 time period and on acceleration from relativistic (~ 2 MeV) to ultra-relativistic energies of 7.7 MeV. The overview of the considered time period is given in Figure 20. The evolution of fluxes was measured by the Relativistic Electron-Proton Telescope (REPT) (Baker, Kanekal, Hoxie, Batiste, et al., 2013) on the Van Allen Probes. During the first storm, beginning on October 9, considered also in a number of previous studies (Reeves et al., 2013; Thorne et al., 2013), the electrons were accelerated to extremely high energies of 7.7 MeV. The second geomagnetic storm that occurred on October 13, resulted in a dropout at ultra-relativistic energies followed by a quick acceleration and subsequent gradual buildup of fluxes for a very broad range of energies. The dynamics of the relativistic and ultra-relativistic electrons observed during these 2 weeks presented the most interesting period for a detailed study.

Identification of the dominant acceleration mechanisms can be conducted by examining the profiles of PSD. The global picture can be obscured by the uncertainties associated with the conversion from fluxed to PSD introduced by the magnetic field models. If one looks at individual energies, it is hard to see a global picture in the peaks of PSD and to combine data from different time periods.

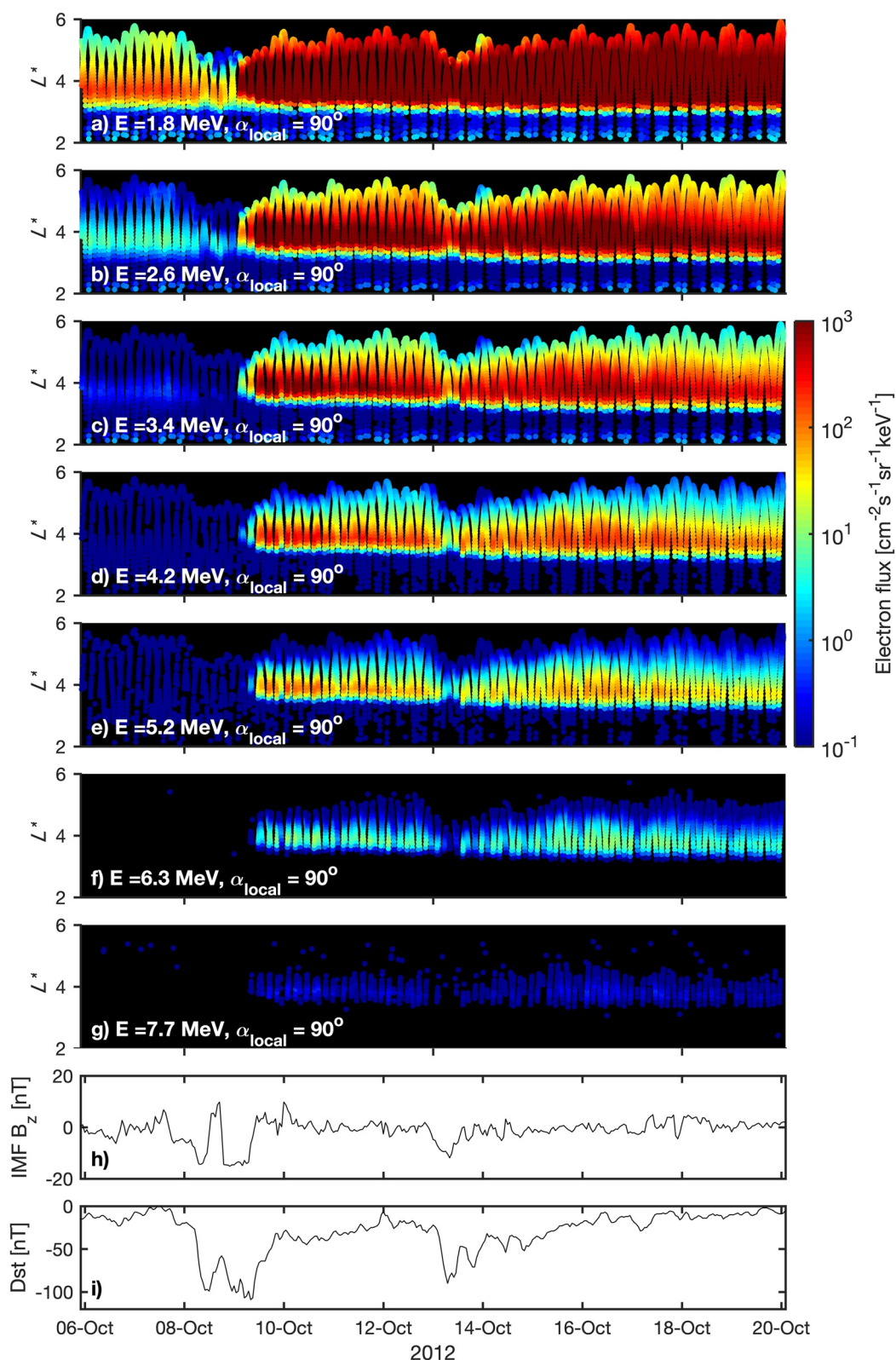


Figure 20. An overview of the radiation belt electron fluxes during October 2012: Panels (a–g) show the differential electron flux measured on Van Allen Probes A and B for electron kinetic energies from 1.8 to 7.7 MeV, at 90° local pitch angle and L-value. Panel (h) shows the evolution of the vertical component of the interplanetary magnetic field (IMF B_z), (i) the evolution of the Dst index [Adopted & Allison & Shprits, 2020].

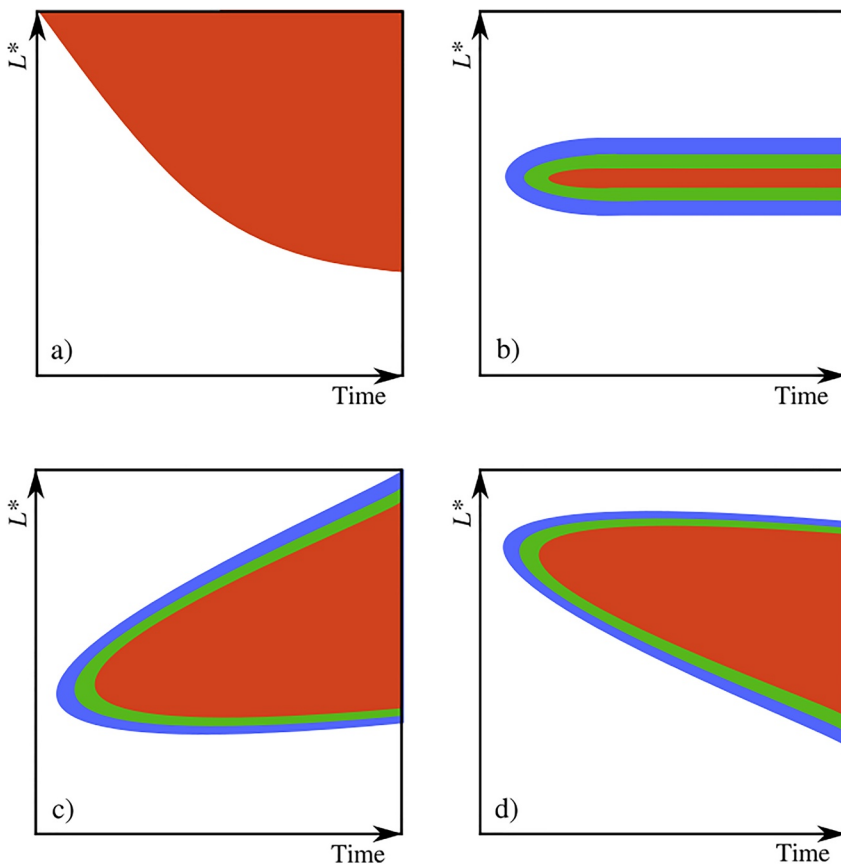


Figure 21. Contours outlining the area in time L-shell space where PSD is within a factor 5 of the maximum value of the phase space density for a chosen values of the first and second adiabatic invariants. The colors blue, green and red correspond to increasing values of the first invariant. The panels show different scenarios (a) inward radial diffusion; (b) local acceleration; (c) local acceleration creating a local peak followed by the outward diffusion; and (d) local acceleration creating a peak followed by the inward diffusion.

To mitigate these limitations, Allison & Shprits (2020) suggested a new way to look at the contours of PSD. To see the global picture of the energization, the authors have not only analyzed the individual profiles of PSD at various values of the first and second adiabatic invariants, but they have also looked at the global picture of acceleration at different energies. To show evolution at different energies, they decided not to plot the entire PSD radial profile but instead outline contours of the regions in the L-time space that are within a factor five of the maximum PSD. Such plots allow to track the behavior of the profiles of PSD at different energies and compare them to each other.

In the case where profiles of PSD are produced by the inward radial diffusion, the profiles are monotonic, and the peak value is reached at the highest observed L-shell. Radial diffusion results in a decrease of the gradient in PSD and hence the inward motion of the inner boundary of the considered area (Figure 21a). As radial diffusion rates are likely to be the same at different energies if the initial shape of the radial profile of PSD is the same at different energies, the contours at different μ will simply overlap each other.

Local acceleration producing local peaks, would result in a fully enclosed area. Moreover, in the case of local acceleration, the peaks should appear first at lower energy and then at higher energy, and contours covering the area within a factor of 5 of the peak of PSD should show the same trend (Figure 21b). The lower μ areas should encompass the contours for higher μ values, and in general the contours at higher μ should appear after the contours at lower μ , demonstrating that energy diffusion would first affect lower energy and after some time, enhance the highest energy ultra-relativistic electrons. If the radial diffusion cannot significantly contribute during the time when local acceleration is operating, the peaks should appear at approximately the same L-shell (Figure 21b). If local acceleration is followed by outward radial diffusion, the enclosed area produced by the

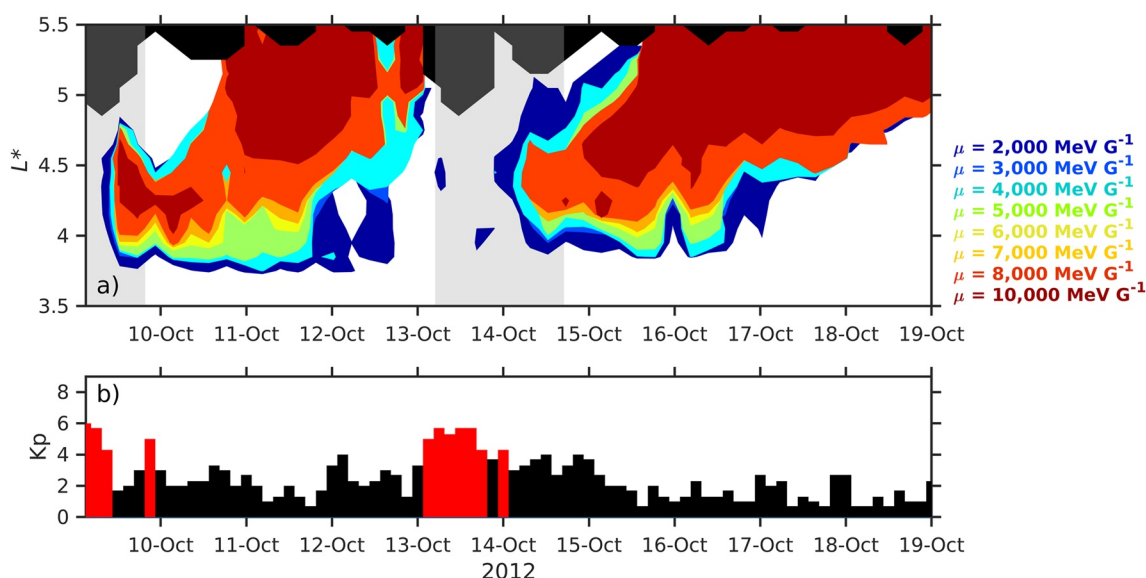


Figure 22. Evolution of maximums in PSD. (a) Evolution of contours within a factor of 5 of the maximum values of PSD during October 2012. Contours are plotted for μ from 2,000 MeV/G to 10,000 MeV/G. By overplotting these contours for different values of the first invariant, the local acceleration over a broad range of energy is revealed. For both storms, acceleration starts at low energy between $L^* \approx 4.0 - 4.5$ and propagates at approximately the same L^* to $\mu = 8,000$ MeV/G and 10,000 MeV/G corresponding to $\sim 5.4 - 6.5$ MeV and $\sim 6.0 - 7.3$ MeV respectively. (b) Kp index. Kp less than four is shown as black bars, and Kp greater than four is shown as red bars [Adopted from Allison & Shprits, 2020].

peak would widen, and the upper boundary would move to higher L -shells (Figure 21c). In the case of two-step acceleration to >3 MeV, suggested by Zhao et al. (2019) and Katsavrias et al. (2019), the inward radial diffusion would follow the local acceleration, and the inner boundary would move inwards. While in reality many of these processes occur simultaneously, such as inward and outward radial diffusion, this diagram can be used as a guide to determine the dominant processes occurring during different stages of the storms.

The temporal evolution of contours within a factor of 5 of the peak PSD, as discussed in Figure 21 during October 2012, is shown in Figure 22. For the considered storms, the contours outline the enclosed area indicating the presence of the peaks. During the initial acceleration, the energization first occurs at 2000 MeV/G and then gradually trickles down to 10 MeV/G, corresponding to ultra-relativistic energies. Note that peaks appear at roughly the same radial distance within $\sim 0.5 R_E$, indicating that acceleration is dominated by the local acceleration and the inward radial diffusion does not significantly contribute to the initial acceleration. Contours are concentric, with lower μ contours encompassing higher μ contours, and do not extend to the highest L^* value for which observations are available (black region). For both of the storms, after peaks are formed and electrons are accelerated to ~ 8 MeV, contours around the peak of fluxes move upwards and broaden after $\sim 2 - 3$ days, consistent with the outward radial diffusion of the locally accelerated electrons scenario, as shown in Figure 18c. There are also visible signatures of concurrent inward radial diffusion, which may move locally accelerated electrons by $\sim 0.5 - 1 R_E$, but such inward motion would correspond to acceleration by $\sim 0.5 - 1$ MeV, which cannot explain the appearance of the ultra-relativistic electrons in the belts. The small radial displacement by less than $0.5 R_E$ may be due to a combination of the inward diffusion and loss in the outer region.

While the results shown in Figure 22 clearly demonstrate that electrons can be accelerated to such a high energy by local diffusion, it still remained unclear why such acceleration occurred only during selected storms. Figure 23 shows an overview of the electron flux at relativistic and ultra-relativistic energies measured on RBSP-A. Only measurements above the background noise of the instrument are displayed. While relativistic electrons of 1.8 MeV show a consistent intensification of fluxes for practically all of the strong storms, ultra-relativistic electrons often do not show any intensifications above the instrument's background levels. The density observations shown in Figure 23c, obtained from the RBSP-A's EMFISIS data and using the Neural-network-based Upper hybrid Resonance Determination (NURD) algorithm (Zhelavskaya et al., 2016), hold the key to the question of the special conditions necessary for the acceleration of electrons to such high energies. Comparison of density

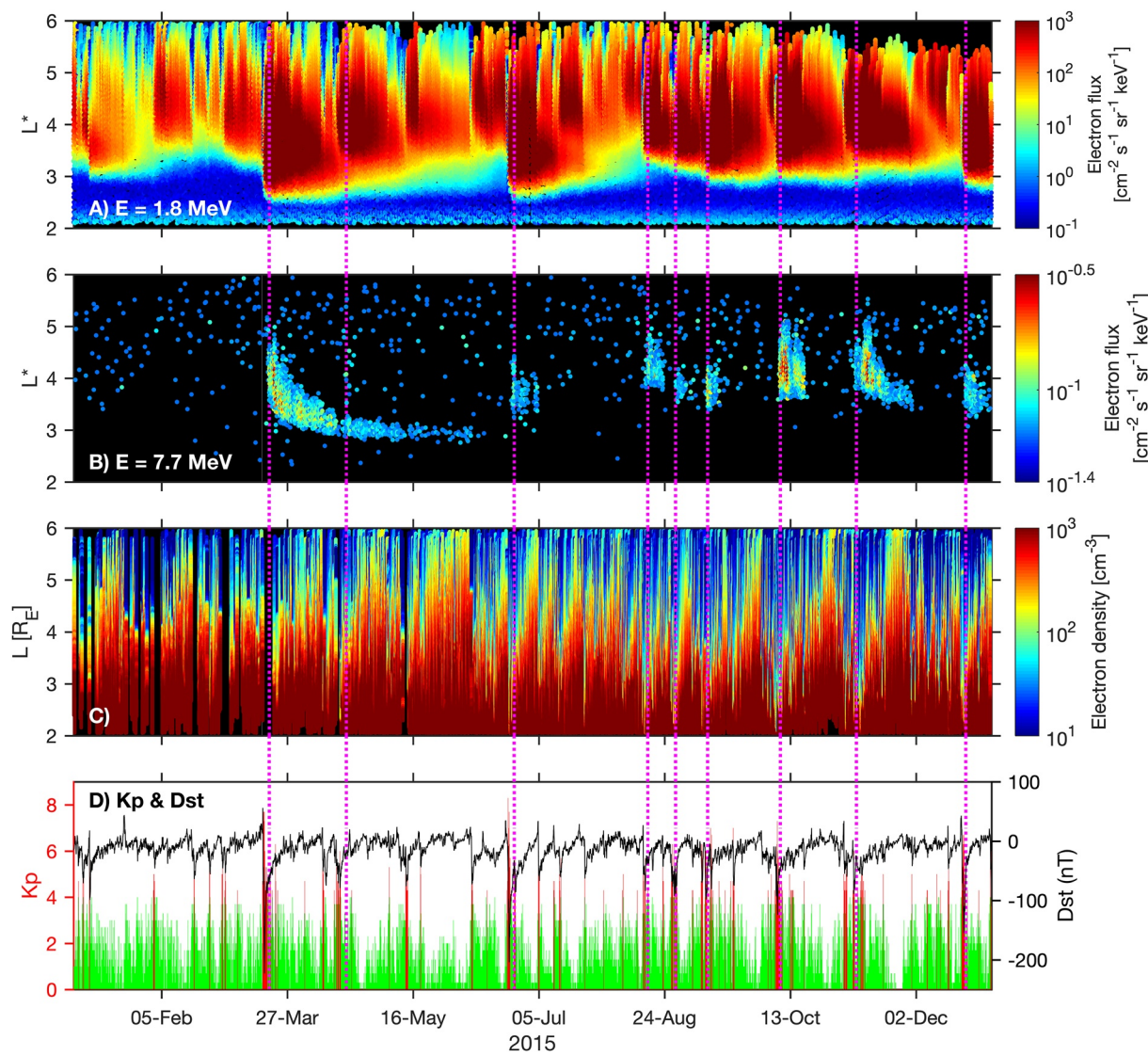


Figure 23. An overview of the relativistic and ultra-relativistic electron fluxes along with electron number density and evolution of Kp and Dst for 2015. The electron flux is presented at a 90° local pitch angle, and kinetic energy of (a) 1.8 MeV, and (b) at 7.7 MeV (c) Electron number density obtained using the NURD and EMFISIS data, (d). Kp and Dst indices. Kp values above four are indicated by the red color. Magenta dotted lines correspond to 7.7 MeV.

evolution with the occurrence of ultra-relativistic electron enhancement, demonstrates that these enhancements occur only when density is depleted (see also Allison et al., 2021).

A more detailed picture can be obtained if we look at the density evolution and timing of 7.7 MeV enhancements for an L-shell of four in the heart of the outer zone.

Figure 24 shows that the average values obtained with the three considered models are very close and consistent with each other. While statistical values of the NURD data set are the same as that of Denton and Sheeley models (Figure 24), there are significant differences between the instantaneous values and statistical models Figure 25. In particular, the density often drops by up to an order of magnitude down to only a few particles per cubic centimeter. There are a number of such depletions throughout the considered time period from October 2012 to October 2017, and it is rather remarkable that most of the intensifications of the 7.7 MeV, shown by magenta lines, occur when the density dropped below 10 cm^{-3} . Note that the dropouts when the seed fluxed of electrons where not enhanced are not showed on Figure 25. The drop in density is certainly not a sufficient condition for the acceleration to multi-MeV energies but it appears to be a necessary condition. At least most of the intensifications to 7.7 MeV require low density values. It also appears that the presence of the seed population is another necessary

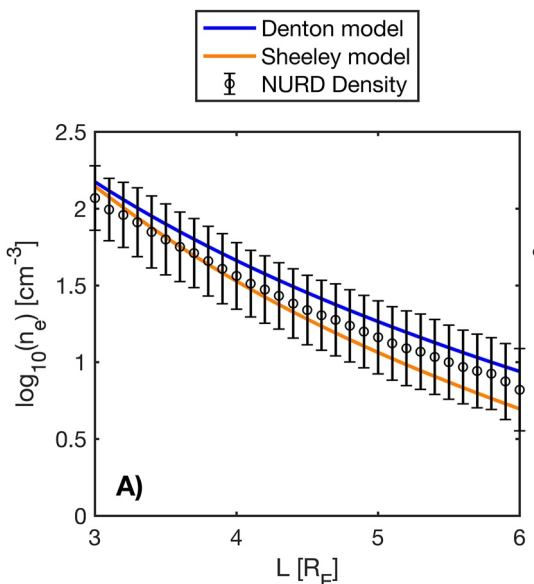


Figure 24. A comparison of plasma density obtained using NURD statistical plasma density from Denton et al. (2004) (blue line) and Sheeley et al. (2001) (orange line). (A) The average values of the logarithm of electron number density obtained by NURD for L from 3 to 6 along with standard deviations presented as error bars. The Denton et al. (2004) and Sheeley et al. (2001) model for midnight are depicted as blue and orange lines respectively.

demonstrate the profound effect of density on acceleration, and that a dramatic dropout in density down to below 10 cc^{-1} is a necessary condition for acceleration to multi-MeV energies. Note however, that it is not a sufficient condition. Certainly not all dropouts in density result in acceleration to multi-MeV energies. Most of the dropouts in density that are not accompanied by the increases to multi-MeV occur during times of low K_p , when wave activity is weak and there is no seed populations of electrons. As diffusion coefficients depend on the square of the mean wave amplitude, there is a significant dependence of local acceleration on wave intensity. The free energy for waves comes from the low energy electrons that generate waves and therefore another requirement for the local acceleration to be efficient is the presence of such injections. Moreover, the acceleration to 3.4 MeV requires the seed population at MeV.

For most of the storms, the typical time of acceleration to 1 MeV is 1–2 days [for example, Kellerman & Shprits, 2012]. The longer delay of approximately 3 days between the onset of the storm and acceleration of multi-MeV energies is consistent with observations in Figure 26 and 26a storm example is shown in Figure 22. The observed longer time delay between the main phase and appearance of multi-MeV as compared to MeV provides another confirmation that particles are accelerated locally and first reach relativistic and only later ultra-relativistic energies.

4. Discussion

Recent observations from Van Allen Probes, which extended to the previously not very well observed and studied ultra-relativistic energies, showed new morphological structures, such as remnant belts (Baker, Kanekal, Hoxie, Henderson, et al., 2013). The observations also showed sudden acceleration to incredibly high ultra-relativistic energies, long-lasting persistent fluxes, and sudden disappearance of the ultra-relativistic electrons (Baker et al., 2014). These observations provided a unique opportunity to test different theories and to better understand the difference between the relativistic and ultra-relativistic flux populations.

Modeling studies clearly showed that global simulations are not able to reproduce sudden dropouts at multi-MeV which lead to the formation of the vary narrow remnant belts, without involving scattering by EMIC waves

conditions that needs to be satisfied for such efficient acceleration to occur in the heart of the radiation belts. A more detailed investigation of the necessary and sufficient conditions for acceleration to MeV energies and detailed case studies should be a subject of future research.

Most of the previous studies used statistical density models, with the exception of Thorne et al. (2013) who considered only one storm. Figure 26 shows the simulations of the competition between local acceleration and loss during relatively disturbed geomagnetic conditions ($K_p = 4$) using VERB-2D, with the Sheeley et al. (2001) density model. These results are compared to VERB-2D simulations that used a density of 10 cc^{-1} . The same model of waves is used for both of these model runs.

The authors chose the initial condition to be a straight line in log-log space, covering energies from 100 keV to 10 MeV, with a sin of pitch angle assumed for all energies. In the case of the statistical density model, local acceleration allows for energy diffusion of only up to 2–3 MeV over the course of a 3-day simulation. One can clearly see the intensification of 1 MeV flux by an order of magnitude after approximately 2 days (Figure 26b), but the fluxes of 5 and 7 MeV remain unaffected. When the density is decreased to 10 cc^{-1} , Figure 26c shows that the hardening of the spectrum extends to approximately 8 MeV. The 1 MeV electrons are accelerated faster, within approximately 1 day (Figure 26d). The low background density not only changes the rate of acceleration at MeV, but also the range of energies that are affected by the local acceleration. In the case of low plasma density, 5 MeV is substantially accelerated above the initial levels within 2–3 days and by the end of the 3-day simulation, there is also a noticeable increase at 7 MeV.

These simulations are consistent with the observations described above that

conditions that needs to be satisfied for such efficient acceleration to occur in the heart of the radiation belts. A more detailed investigation of the necessary and sufficient conditions for acceleration to MeV energies and detailed case

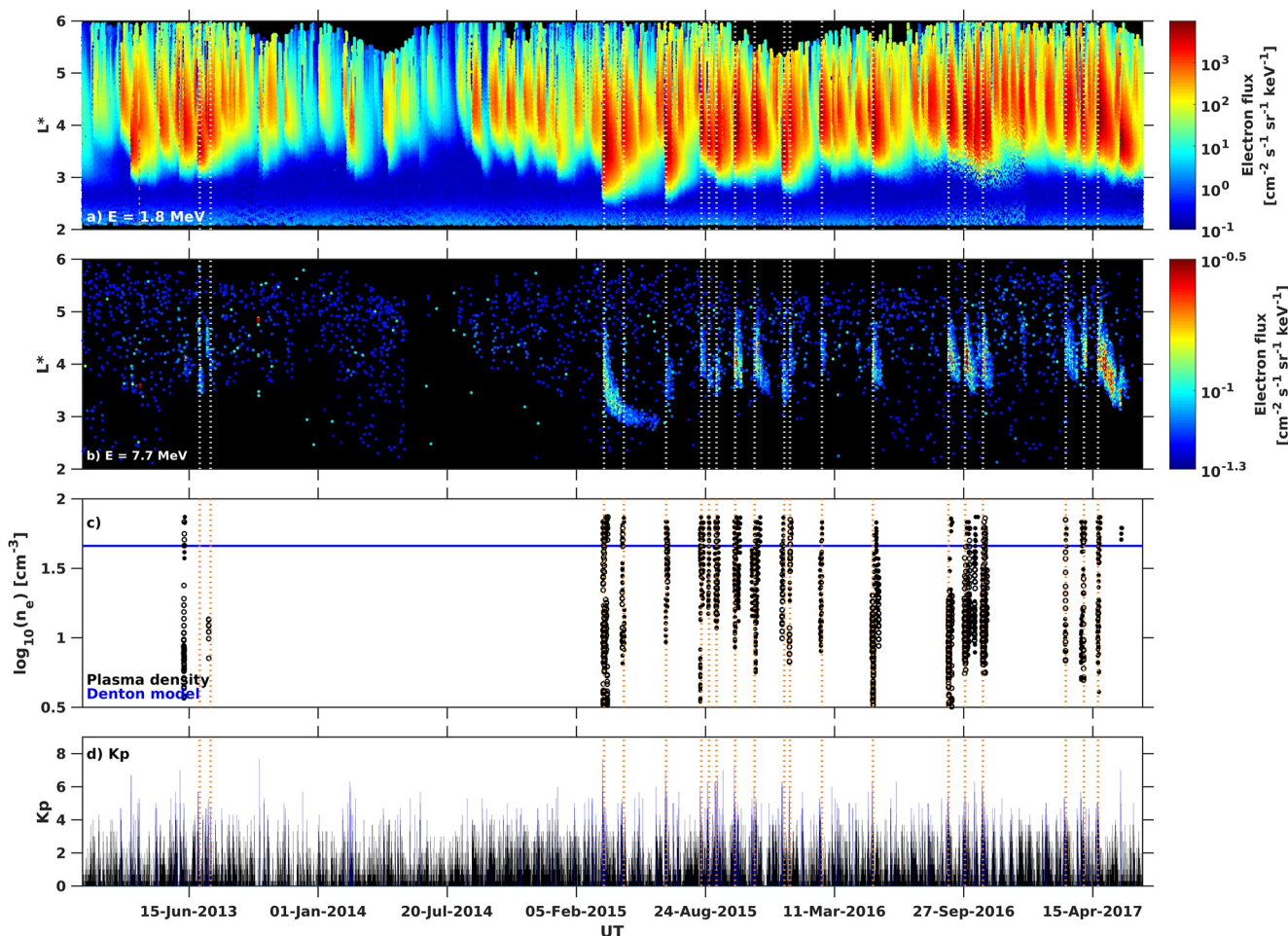


Figure 25. Evolution of 1.8 MeV (a) and 7.7 MeV(b) fluxes from 01-Jan-2013 to 30-Jun-2017. (c) Plasma density at $L = 4$ obtained with NURD (black points). The densities (outside the pp at $L = 4$) shown are restricted to when the 1.8 MeV flux at $L = 4$ is $> 300 \text{ cm}^{-2} \text{ s}^{-1} \text{ sr}^{-1} \text{ keV}^{-1}$ within the following day. Empty circles indicate times when the values of NURD flagged as a low confidence due to interference with other types of waves on the spectrograms. Density predicted by the statistical model of Denton et al. (2004) (blue line). Vertical dotted lines indicate enhancement times of 7.7 MeV electrons. They mark the first time that the 7.7 MeV was above the background threshold for two consecutive passes at $L = 4$ (time then taken as the first of those two pass times). $L = 4$ is defined as ± 0.05 .

(Shprits et al., 2013). Scattering by VLF waves is slower at ultra-relativistic energies than at relativistic energies and cannot explain sudden dropouts. The loss to the magnetopause, caused by outward radial diffusion, can and frequently does, produce very fast dropouts in the outer region of the radiation belts. However, outward radial diffusion acts to smooth the radial profile and cannot reproduce the narrow structures with a width of a fraction of the earth radii, as seen in the Van Allen Probe measurements (Mann et al., 2016).

Observational evidence for the efficiency of the EMIC wave scattering comes from the evolution of the radial profiles of PSD, showing the deepening minima (Shprits et al., 2017, 2018), along with the simultaneous narrowing of the pitch angle distributions (Aseev et al., 2017; Usanova et al., 2014). Both modeling and observations indicated that only multi-MeV are affected by the EMIC waves, while a loss at MeV is not evident. Similarly, theoretical sensitivity studies (Cao et al., 2017) show that only under very special conditions (composition, anisotropy, high background electron density) can EMIC waves potentially resonate with the MeV electrons. It is currently unknown if under certain conditions, EMIC wave scattering may contribute to the loss of MeV electrons, which remains an open research question.

Some of the indirect measurements such as measurements of the balloon x-rays (Blum et al., 2015; Millan et al., 2007; Woodger et al., 2015, 2018) indicated that sub-MeV electrons may be precipitating into the atmosphere. It remains unclear if such precipitation of sub-MeV electrons is due to inaccuracies in the inferior of the spectrum. Also, several studies (Clilverd et al., 2015; Rodger et al., 2015) used the approach of Sandanger

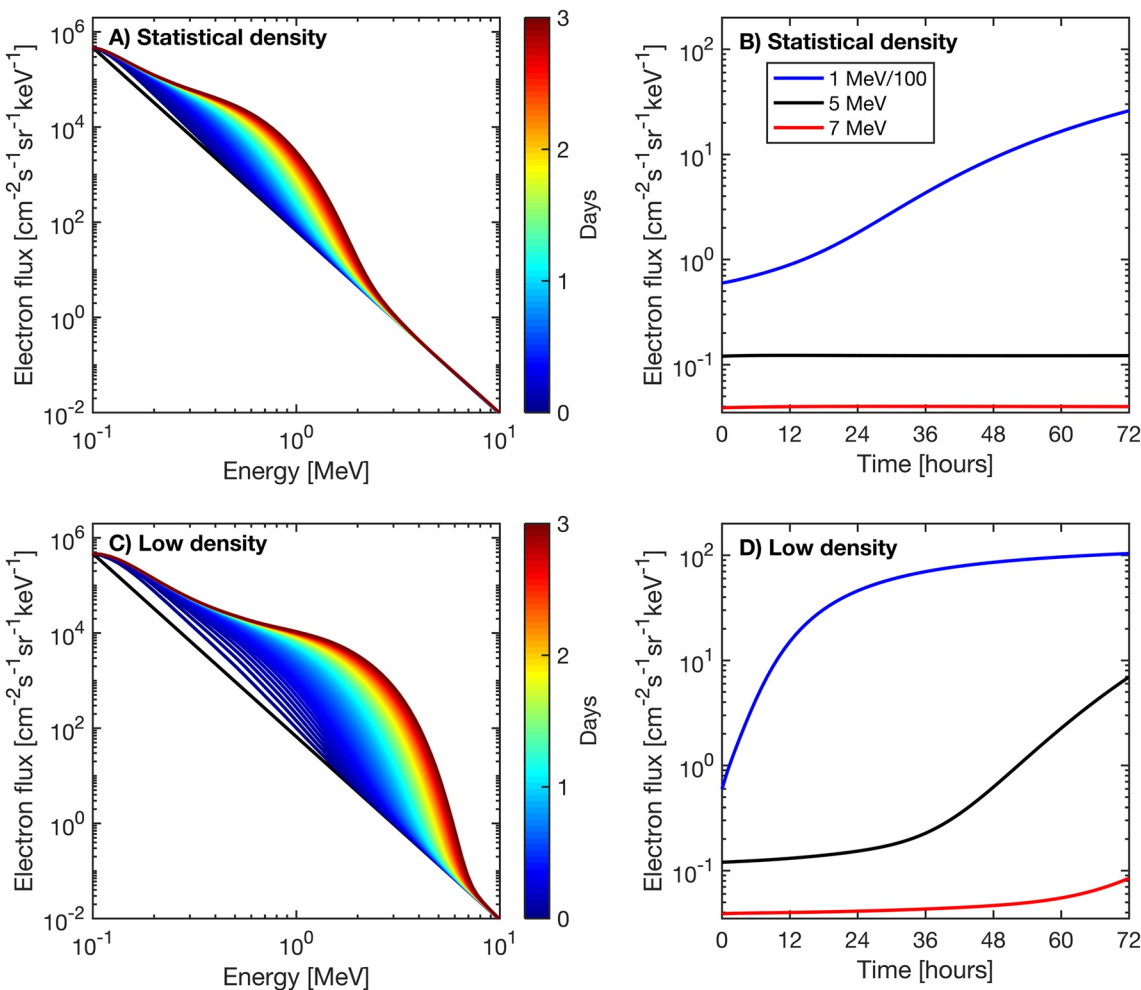


Figure 26. VERB-2D 3-day simulations of the evolution of the electron flux at $L^* = 4$ and pitch angle of 70° . The calculation includes pitch angle, energy, and mixed diffusion. Panels (a) and (b) show a model run, with scattering rates calculated assuming Sheeley statistical density model. Sheeley model predicts a density of 33.7 cc^{-1} at midnight and 44.8 cc^{-1} at noon. (a) and (c) Evolution of the electron energy spectrum color-coded in time for statistical density and density of 10 cc^{-1} respectively. (b) and (d) Evolution of 1, 5, and 7 MeV for the statistical and low-density values respectively. The 1 MeV flux on Figures (b) and (d) is divided by a factor of 100 [Adopted from Allison et al., 2021].

et al., 2009 to identify the loss due to EMIC waves by identifying simultaneous precipitation of ions and electrons. This method may be potentially inaccurate if the precipitation is caused by coincidental precipitation due to, for example, EMIC and chorus waves. Another potential explanation for these observations could potentially be that EMIC waves do scatter sub-MeV electrons but that does not affect a significant number of electrons as compared to total number of electrons at these energies. In that case such precipitation would not significantly alter the dynamics of hundreds of keV particles but may affect the spectrum of precipitating electrons. A weak loss by EMIC waves that is smoothed out by the radial diffusion, may not be so easily seen in the profiles of PSD but may, in theory, contribute to the loss of relativistic electrons.

A recent study by Drozdov et al. (2017) showed how the improved understanding of EMIC wave scattering can help better predict ultra-relativistic electron dynamics and evolution. The main difficulty in modeling the scattering induced by EMIC waves lies in the fact that the minimum resonance energy depends on the spectral properties of waves and also on the plasma composition. EMIC waves may be very strongly localized and require satellites to fortuitously be at the right place and at the right time to measure the amplitudes and spectral properties of waves. Ground measurements can serve as a guide but cannot be used to precisely determine the amplitudes, location, and spectral properties of waves. The difference between MeV and multi-MeV morphology and dynamics is

partially due to the pronounced effect of EMIC wave scattering, which can empty the multi-MeV outer belt and produce very sharp boundaries between the regions affected and not affected by the EMIC-induced scattering.

As discussed in the introduction of this review, radial diffusion plays a most important role in accelerating electrons to MeV energies. The simplified simulations including only radial diffusion and neglecting local acceleration are capable of predicting the general structure of the belts (Shprits & Thorne, 2004; Shprits et al., 2005; Shprits, Thorne, Friedel et al., 2006). While local acceleration can assist the radial diffusion and produce the build ups of fluxes often seen in the recovery phase of the storm, the simulations of local acceleration also without a supply of seed population by radial diffusion would not be able to reproduce even the general dynamics of the belts. The importance of local acceleration increases with increasing energy. The acceleration from MeV to ultra-relativistic energies occurs mostly due to local acceleration and not due to a combination of both radial diffusion and local acceleration. PSD radial profiles, along with combined contour outlining the regions around maximum values of PSD (Allison & Shprits., 2020), clearly show that at least for the events considered, the local acceleration was by far the dominant mechanism that is responsible for the acceleration of electrons from MeV up to 7.7 MeV. The contours around the maximum value of PSD show that acceleration occurred approximately at the same radial distance from the Earth, with a few MeV appearing first, followed by the higher energy. Observations of the electron number density together with 7.7 MeV fluxes show that intensifications in fluxes above the REPT background levels occur only when plasma density drops below 10 per cubic centimeter, which is much lower than the statistical value. Considering that these electrons are accelerated locally, such dependence is not surprising, as local acceleration is more efficient in low-density regions (Horne et al., 2005) and, in such low-density regions, electrons can be accelerated up to ultra-relativistic energies while for the median values of density, local acceleration can only accelerate electrons in energies up to 2–3 MeV (see Figure 21). The precise boundary between the ultra-relativistic and relativistic populations can not be clearly defined and left intentionally vague in this study. There are clear differences in dynamics between the 1–2 MeV electrons and above 5 MeV electrons, but it is difficult to say where is the boundary between relativistic and ultra-relativistic electrons. Similarly, to difficulties with the exact demarcation of the ring current and the radiation belts, it isn't easy to define a unique value of energy that separates the relativistic and Multi-MeV or ultra-relativistic election population.

In Allison et al., 2021, discussed above, the effect of global background plasma density depletions were considered. Dropouts in density over a small special region may also play a role. Localized density depletion can form a so-called low-density duct [for example, Streltsov et al., 2006]. The density duct can confine the VLF waves and contribute to the acceleration of energetic electrons.

It still remains unclear if the acceleration to multi-MeV energies can be fully described by the quasi-linear diffusion or whether a non-linear treatment of the particle acceleration [for example, Artemyev et al., 2017; Albert, 2010; Karpman & Shklyar, 1972; Katoh et al., 2008 Nunn, 1971; Omura et al., 2015; Shklyar & Matsumoto, 2009] or additional non-linear advective terms [for example, Artemyev et al., 2021] are required to reproduce observations. For large wave amplitudes it has been shown that the quasi-linear approach is not appropriate (Shapiro & Sagdeev, 1997). Some studies suggest that coherent chorus waves can accelerate 10–100 keV electrons up to several MeV energies by non-linear trapping processes called relativistic turning acceleration (RTA) (Omura et al., 2007) and ultra-relativistic acceleration (URA) (Summers & Omura, 2007). The non-linear trapping occurs for resonant electrons with a limited range of gyro-phase and specific timing of encountering a wave packet. Omura et al. (2015) formulated a numerical Green's function method of modeling the non-linear acceleration of energetic electrons. When the wave normal angles of chorus waves become oblique through propagation, the nonlinear trapping of energetic electrons moving in the same direction of a wave packet also takes place through Landau resonance, and the electrons are rapidly accelerated to about 2 MeV within tens of chorus emissions [Hsieh & Omura, 2017; Omura et al., 2019; Hsieh et al., 2020]. Hiraga and Omura (2020) performed test particle simulations to investigate the acceleration mechanism of relativistic electrons through interaction with multi-subpacket chorus waves. They found that successive trapping of the resonant electrons can cause the efficient accelerations from the consecutive multiple subpackets of a chorus wave element. However, since electrons exhibit adiabatic fluctuations that are difficult to exactly quantify, it is difficult to identify the observational evidence of non-linear wave-particle acceleration. Most of the studies of non-linear wave particle acceleration predict faster acceleration rates than can be provided by quasi-linear theory, the addition of systematic faster acceleration would certainly produce systematic overestimation of the fluxes. Understanding the success of quasi-linear simulations as well as the limitations of this approach should be a subject of future research. The

timing of acceleration may be a good of good check of validity of a given acceleration mechanism. Quasi-linear modeling presented in this study on Figure 26 occurs on the time-scale of 3 days which is consistent with observations presented on Figure 22. More detailed analysis of multiple events and comparison with non-linear simulations should be a subject of future research.

Prompt acceleration can be also produced by shocks. Shock-induced acceleration of radiation belt electrons has been observed during storms by CRRES (Blake et al., 1992; X. Li et al., 1993), Cluster (Zong et al., 2009) and Van Allen Probes (Foster et al., 2015; Hudson et al., 2017; Hao et al., 2019). However, such events are rare and cannot explain most of the dynamic variability of the radiation belts.

To understand to what extent quasi-linear simulations can reproduce the dynamics of the 1MeV radiation belt electrons, here we perform a long-term Fokker-Planck simulation for the Van Allen Probe era during the years from October 2012 to December 2017 using the VERB-3D quasi-linear diffusion code with wave models inferred from Van Allen Probes measurements (Wang et al., 2019; Wang & Shprits, 2019; Wang et al., 2020). In this simulation, we do not use any of the measurements from the Van Allen Probes for setting up the boundary conditions. We use GOES data at GEO as the only data input for outer L^* boundary condition. Then we validate our simulations results against Van Allen Probe observations. To compare the simulation results directly with the satellite observations, we ‘fly’ virtual Van Allen Probes A and B spacecraft through the simulation results, and predict the flux at exact the energy and pitch-angle that Van Allen Probes measure. Figure 27 shows an example at 0.9 MeV and 57.3° local pitch-angle. To compare the flux from observations (J_o) with the flux from the simulation (J_s), we calculate the difference between J_s and J_o normalized by the maximum flux for fixed pitch-angle and energy and over all values of L^* over an 8-hr time window. We do this normalization in order to concentrate on the difference where the peaks of flux are observed. For small flux near the slot region, the difference can be several orders of difference. However, such large ratios of two very small numbers are not physically interesting as this region is effectively devoid of energetic particles. Moreover, observations may be inaccurate when the fluxes are low and close to background levels of the instruments. The equation for calculating the normalized difference (ND_{max}) following (Subbotin & Shprits, 2009) is given as:

$$ND_{max}(L^*, t) = \frac{J_s(L^*, t) - J_o(L^*, t)}{\max_{\text{over } L^* \text{ every 8 hours}} \frac{J_s(L^*, t) + J_o(L^*, t)}{2}} \quad (1)$$

Considering the number of uncertainties and assumptions that are made in the code it is rather remarkable (Figure 27c) how well the VERB-3D code can reproduce the dynamics of the belts. During the individual storms there are of course differences that may potentially be due to missing physical process such as non-linear interactions but also may be due to the assumptions of the code. As described above in this study one of such assumptions is a constant density that as clearly shown on Figure 22 is not satisfied for many storms that result in the acceleration to multi-MeV energies. The assumption of the statistical density that is constant in time is most important for the ultra-relativistic electrons. In particular, the VERB-3D code currently cannot reproduce the acceleration to such high energies as that requires very low values of the plasma density. Such accelerated electrons would also be piling up in the code that does not include EMIC scattering (e.g., Drozdov et al., 2019) that occurs in the regions of plumes and in the plasmasphere. Such improvements to the existing codes should be a subject of future work and are required to reproduce the dynamics of the ultra-relativistic electrons.

Figure 28 shows the values of energy across radial distance calculated for various values of the first invariant at $K = 0.01 G^{0.5} R_E$, $K = 0.1 G^{0.5} R_E$, and $K = 0.3 G^{0.5} R_E$ in a dipole magnetic field model. For the value of K shown in Figure 25b, the 8 MeV energy at $L = 4$ corresponds to $\mu = 10,000$ MeV/G. If these electrons were accelerated by radial diffusion, they would need to have the energy of ~4 MeV at $L = 6$ and an energy of ~2 MeV at $L = 8$. It is also not likely that electrons can gain several MeV in energy from local acceleration around and beyond geosynchronous equatorial orbit (GEO), as the magnetic field becomes weak, increasing the plasma to gyrofrequency ratio and making local acceleration inefficient. Even if they would reach such energy, their drift pass is likely to take them out of the magnetosphere into the interplanetary medium.

Radial diffusion will of course, be operational after the peaks are formed by local acceleration (Reeves et al., 1998) and will redistribute accelerated particles inwards below the peak in PSD and outwards outside of the peak. Radial diffusion will also help accelerate relativistic electrons that form the seed population for the local acceleration to multi-MeV. It should also be noted that the outward radial diffusion does play a major role even at multi-MeV, by

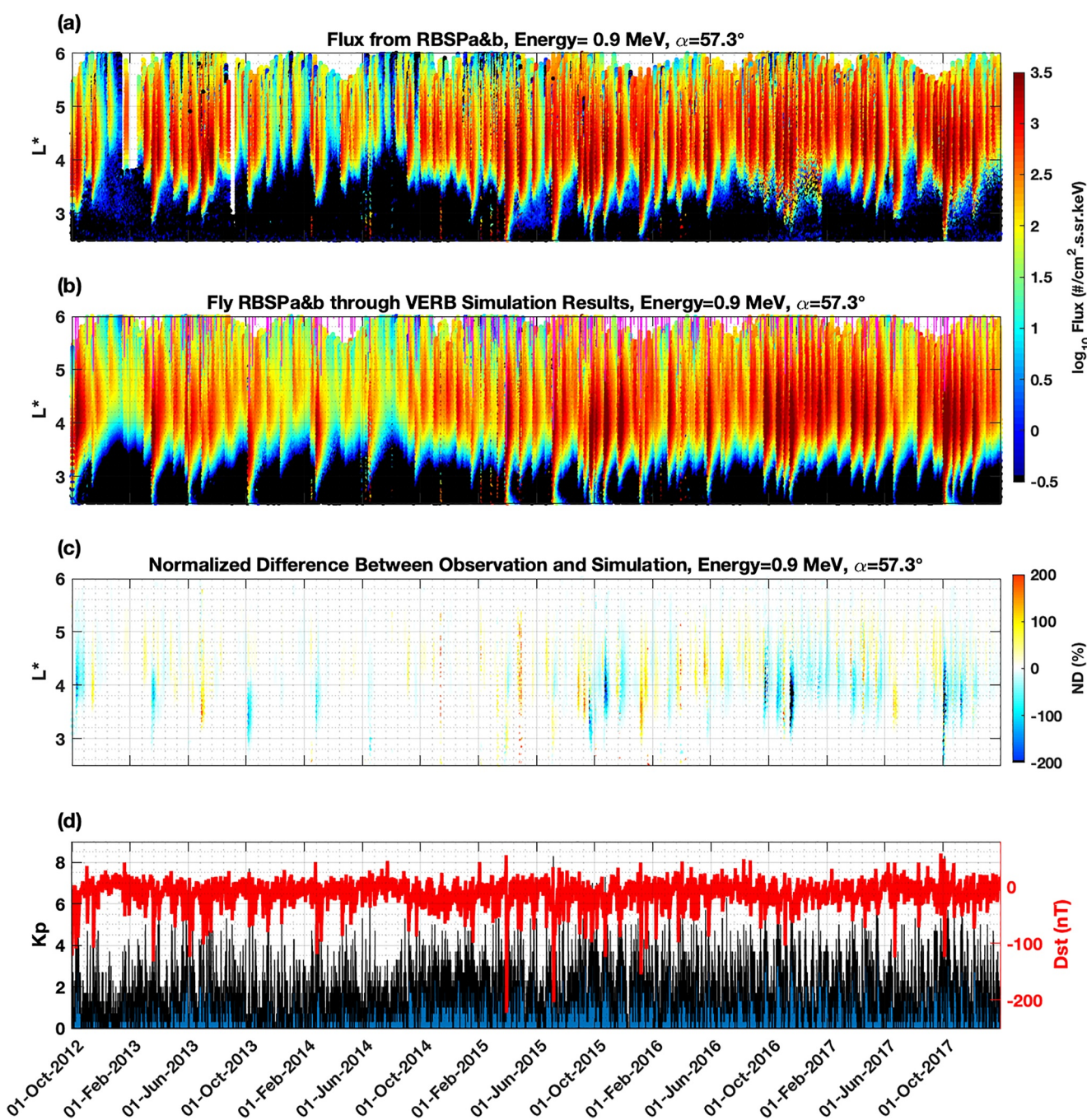


Figure 27. Comparison of Van Allen Probe observations with a fly-through of virtual Van Allen Probes spacecra... Panel (a) shows the electron flux observed by Van Allen Probes, while panel (b) shows the results from the satellite ‘fly-through’ of the simulation. The overplotted magenta line in panel (b) shows the last closed drift shell position calculated in T04s magnetic field model using the ONERA IRBEM library. The positions of the last closed drift shell are used to simulate the magnetopause shadowing effect, as done in Wang and Shprits (2019) and Wang et al. (2020). Panel (c) shows the normalized difference as described by Equation 1 and panel (d) shows the evolution of the Kp and Dst indices of geomagnetic activity.

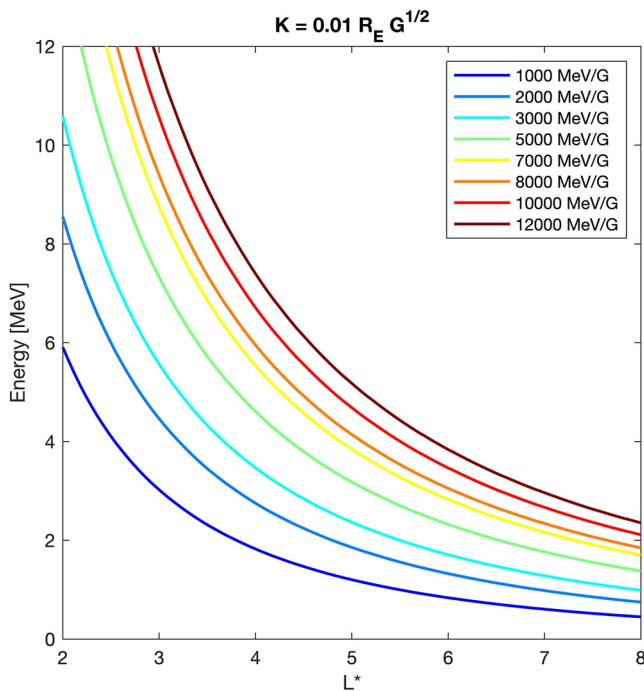


Figure 28. Energy and L^* calculated in the geomagnetic dipole field for various values of the first adiabatic invariants μ (colored lines) at $K = 0.01 G^{0.5} R_E$.

bringing these most energetic electrons accelerated in the heart of the belts outwards and populating the outer regions near GEO.

5. Conclusions

There are certainly several similarities between the physical processes that determine the evolution of relativistic and ultra-relativistic electrons. Outward radial diffusion, driven by loss to the magnetopause, would affect all energies. Local acceleration and radial diffusion can also operate at relativistic and ultra-relativistic energies. However, there are also many differences: (a) EMIC wave scattering becomes important for the multi-MeV electrons, whilst not significantly affecting MeV electrons, and can produce very narrow remnant belts (e.g., Baker, Kanekal, Hoxie, Henderson, et al., 2013, 2014); (b) the acceleration events occur much more rarely for the ultra-relativistic particles than for relativistic particles and require very low background plasma density; (c) VLF waves such as hiss and chorus are less efficient in scattering ultra-relativistic electrons than relativistic electrons, which allow multi-MeV electrons to persist for a very long time. Based on the analysis of the evolution of the radiation belts in September 2012 and the analysis of the differences in loss processes, Shprits et al. (2013) suggested that ultra-relativistic electrons should be classified as a different population from the MeV radiation belt electrons. This manuscript presents several examples, including analysis of pitch angle distributions, angular distribution, energy spectrum, wave data, and modeling, which provide convincing support for this original speculation.

Results presented in this review demonstrate that the coldest part of the spectrum has a most pronounced effect on the most energetic particles in the tail of the energy distribution. The efficient loss due to EMIC waves occurs only in the high-density regions inside the plasmasphere or in the regions of plumes where densities exceed hundreds or thousands of particles per cubic centimeter. In contrast, acceleration occurs only when the plasma is extremely tenuous with densities below 10 particles per cubic centimeter.

The difference in the acceleration (continuous acceleration for MeV and sudden acceleration, when density is very low, at multi-MeV), difference in loss (loss by VLF waves at MeV and very fast loss by EMIC waves at multi-MeV) together with observations of different evolution and morphological structures, justify classifying ultra-relativistic electrons as a population different from the bulk populations of the radiation belts. Similar to how the ring current is considered a population different from the radiation belts, multi-MeV electrons form a new population that co-exists with the relativistic outer electron radiation zone.

Data Availability Statement

The Van Allen Probes data used to generate figures in the original publications is freely available at <https://rbspgw.jhuapl.edu/>.

Acknowledgments

This project has received funding from the European Union's Horizon 2020 research and innovation program under grant agreement no. 870452 (PAGER). The author would like to thank the Van Allen Probes Science team for providing data that was used in different studies that were discussed in the review paper. The author would also like to acknowledge support from NASA grant 80NSSC18K0663. Open access funding enabled and organized by Projekt DEAL.

References

- Albert, J. M. (2003). Evaluation of quasi-linear diffusion coefficients for EMIC waves in a multispecies plasma. *Journal of Geophysical Research*, 108(A6). <https://doi.org/10.1029/2002JA009792>
- Albert, J. M. (2005). Evaluation of quasi-linear diffusion coefficients for whistler mode waves in a plasma with arbitrary density ratio. *Journal of Geophysical Research*, 110(A3). <https://doi.org/10.1029/2004JA010844>
- Albert, J. M. (2010). Diffusion by one wave and by many waves. *Journal of Geophysical Research*, 115. <https://doi.org/10.1029/2009JA014732>
- Albert, J. M., & Young, S. L. (2005). Multidimensional quasi-linear diffusion of radiation belt electrons. *Geophysical Research Letters*, 32(14). <https://doi.org/10.1029/2005GL023191>
- Allison, H. J., & Shprits, Y. Y. (2020). Local heating of radiation belt electrons to ultra-relativistic energies. *Nature Communications*, 11(1), 4533. <https://doi.org/10.1038/s41467-020-18053-z>

- Allison, H. J., Shprits, Y. Y., Zhelavskaya, I. S., Wang, D., & Smirnov, A. G. (2021). Gyroresonant wave-particle interactions with chorus waves during extreme depletions of plasma density in the Van Allen radiation belts. *Science Advances*, 7(5), eabc0380. <https://doi.org/10.1126/sciadv.abc0380>
- Artemyev, A. V., Neishtadt, A. I., Vasiliev, A. A., & Mourenas, D. (2017). Probabilistic approach to nonlinear wave-particle resonant interaction. *Physical Review E*, 95(2), 023204.
- Artemyev, A. V., Neishtadt, A. I., Vasiliev, A. A., Zhang, X., Mourenas, D., & Vainchtein, D. (2021). Long-term dynamics driven by resonant wave-particle interactions: From Hamiltonian resonance theory to phase space mapping. *Journal of Plasma Physics*, 87(2), 835870201. <https://doi.org/10.1017/S0022377821000246>
- Aseev, N. A., Shprits, Y. Y., Drozdov, A. Y., Kellerman, A. C., Usanova, M. E., Wang, D., & Zhelevskaya, I. S. (2017). Signatures of ultrarelativistic electron loss in the heart of the outer radiation belt measured by Van Allen Probes. *Journal of Geophysical Research: Space Physics*, 122(10), 10102–10111. <https://doi.org/10.1002/2017JA024485>
- Baker, D. N., Jaynes, A. N., Hoxie, V. C., Thorne, R. M., Foster, J. C., Li, X., et al. (2014). An impenetrable barrier to ultrarelativistic electrons in the Van Allen radiation belts. *Nature*, 515(7528), 531–534. <https://doi.org/10.1038/nature13956>
- Baker, D. N., Kanekal, S. G., Hoxie, V. C., Batiste, S., Bolton, M., Li, X., et al. (2013). The relativistic electron-proton telescope (REPT) instrument on board the radiation belt storm Probes (RBSP) spacecraft: Characterization of Earth's radiation belt high-energy particle populations. *Space Science Reviews*, 179(1), 337–381. <https://doi.org/10.1007/s11214-012-9950-9>
- Baker, D. N., Kanekal, S. G., Hoxie, V. C., Henderson, M. G., Li, X., Spence, H. E., et al. (2013). A long-lived relativistic electron storage ring embedded in Earth's outer Van Allen Belt. *Science*, 340(6129), 186–190. <https://doi.org/10.1126/science.123518>
- Blake, J. B., Kolasinski, W. A., Filius, R. W., & Mullen, E. G. (1992). Injection of electrons and protons with energies of tens of MeV into L less than 3 on 24 March 1991. *Geophysical Research Letters*, 19, 821–824. <https://doi.org/10.1029/92GL00624>
- Blum, L. W., Halford, A., Millan, R., Bonnell, J. W., Goldstein, J., Usanova, M., et al. (2015). Observations of coincident EMIC wave activity and duskside energetic electron precipitation on 18–19 January 2013. *Geophysical Research Letters*, 42(14), 5727–5735. <https://doi.org/10.1002/2015GL065245>
- Blum, L. W., Remya, B., Denton, M. H., & Schiller, Q. (2020). Persistent EMIC wave activity across the nightside inner magnetosphere. *Geophysical Research Letters*, 47(6), e2020GL087009. <https://doi.org/10.1029/2020GL087009>
- Borovsky, J. E., & Shprits, Y. Y. (2017). Is the Dst index sufficient to define all geospace storms? *Journal of Geophysical Research: Space Physics*, 122(11), 11543–11547. <https://doi.org/10.1002/2017JA024679>
- Boyd, A. J., Spence, H. E., Huang, C.-L., Reeves, G. D., Baker, D. N., Turner, D. L., et al. (2016). Statistical properties of the radiation belt seed population. *Journal of Geophysical Research: Space Physics*, 121(8), 7636–7646. <https://doi.org/10.1002/2016JA022652>
- Cao, X., Shprits, Y. Y., Ni, B., & Zhelevskaya, I. S. (2017). Scattering of ultra-relativistic electrons in the Van Allen radiation belts accounting for hot plasma effects. *Scientific Reports*, 7(1), 17719. <https://doi.org/10.1038/s41598-017-17739-7>
- Carpenter, D. L., & Anderson, R. R. (1992). An ISEE/whistler model of equatorial electron density in the magnetosphere. *Journal of Geophysical Research*, 97(A2), 1097–1108. <https://doi.org/10.1029/91JA01548>
- Cervantes, S., Shprits, Y. Y., Aseev, N. A., & Allison, H. J. (2020). Quantifying the effects of EMIC wave scattering and magnetopause shadowing in the outer electron radiation belt by means of data assimilation. *Journal of Geophysical Research: Space Physics*, 125(8), e2020JA028208. <https://doi.org/10.1029/2020JA028208>
- Chen, L., Zhu, H., & Zhang, X. (2019). Wavenumber analysis of EMIC waves. *Geophysical Research Letters*, 46, 5689–5697. <https://doi.org/10.1029/2019GL082686>
- Chen, Y., Reeves, G. D., & Friedel, R. H. W. (2007). The energization of relativistic electrons in the outer Van Allen radiation belt. *Nature Physics*, 3(9), 614–617. <https://doi.org/10.1038/nphys655>
- Chilverd, M. A., Duthie, R., Hardman, R., Hendry, A. T., Rodger, C. J., Raita, T., et al. (2015). Electron precipitation from EMIC waves: A case study from 31 May 2013. *Journal of Geophysical Research: Space Physics*, 120, 3618–3631. <https://doi.org/10.1002/2015JA021090>
- Denton, R. E., Menietti, J. D., Goldstein, J., Young, S. L., & Anderson, R. R. (2004). Electron density in the magnetosphere. *Journal of Geophysical Research*, 109(A9). <https://doi.org/10.1029/2003JA010245>
- Denton, R. E., Ofman, L., Shprits, Y. Y., Bortnik, J., Millan, R. M., Rodger, C. J., et al. (2019). Pitch angle scattering of sub-MeV relativistic electrons by electromagnetic ion cyclotron waves. *Journal of Geophysical Research: Space Physics*, 124(7), 5610–5626. <https://doi.org/10.1029/2018JA026384>
- Drozdov, A. Y., Aseev, N., Effenberger, F., Turner, D. L., Saikin, A., & Shprits, Y. Y. (2019). Storm time depletions of multi-MeV radiation belt electrons observed at different pitch angles. *Journal of Geophysical Research: Space Physics*, 124(11), 8943–8953. <https://doi.org/10.1029/2019JA027332>
- Drozdov, A. Y., Shprits, Y. Y., Usanova, M. E., Aseev, N. A., Kellerman, A. C., & Zhu, H. (2017). EMIC wave parameterization in the long-term VERB code simulation. *Journal of Geophysical Research: Space Physics*, 122(8), 8488–8501. <https://doi.org/10.1002/2017JA024389>
- Drozdov, A. Y., Usanova, M. E., Hudson, M. K., Allison, H. J., & Shprits, Y. Y. (2020). The role of hiss, chorus, and EMIC waves in the modeling of the dynamics of the multi-MeV radiation belt electrons. *Journal of Geophysical Research: Space Physics*, 125(9), e2020JA028282. <https://doi.org/10.1029/2020JA028282>
- Fälthammar, C.-G. (1965). Effects of time-dependent electric fields on geomagnetically trapped radiation. *Journal of Geophysical Research*, 70(11), 2503–2516. <https://doi.org/10.1029/JZ070i011p02503>
- Fennell, J. F., Claudepierre, S. G., Blake, J. B., O'Brien, T. P., Clemons, J. H., Baker, D. N., et al. (2015). Van Allen Probes show that the inner radiation zone contains no MeV electrons: ECT/MagEIS data. *Geophysical Research Letters*, 42(5), 1283–1289. <https://doi.org/10.1002/2014GL062874>
- Foster, J., Wygant, J., Hudson, M., Boyd, A., Baker, D., Erickson, P., & Spence, H. E. (2015). Shock-induced prompt relativistic electron acceleration in the inner magnetosphere. *Journal of Geophysical Research: Space Physics*, 120, 1661–1674. <https://doi.org/10.1002/2014JA020642>
- Glauert, S. A., & Horne, R. B. (2005). Calculation of pitch angle and energy diffusion coefficients with the PADIE code. *Journal of Geophysical Research*, 110(A4). <https://doi.org/10.1029/2004JA010851>
- Glauert, S. A., Horne, R. B., & Meredith, N. P. (2014). Three-dimensional electron radiation belt simulations using the BAS Radiation Belt Model with new diffusion models for chorus, plasmaspheric hiss, and lightning-generated whistlers. *Journal of Geophysical Research: Space Physics*, 119(1), 268–289. <https://doi.org/10.1002/2013JA019281>
- Glauert, S. A., Horne, R. B., & Meredith, N. P. (2018). A 30-year simulation of the outer electron radiation belt. *Space Weather*, 16(10), 1498–1522. <https://doi.org/10.1029/2018SW001981>
- Green, J. C., & Kivelson, M. G. (2004). Relativistic electrons in the outer radiation belt: Differentiating between acceleration mechanisms. *Journal of Geophysical Research*, 109(A3). <https://doi.org/10.1029/2003JA010153>

- Hao, Y. X., Zong, Q.-G., Zhou, X.-Z., Rankin, R., Chen, X. R., Liu, Y., et al. (2019). Global-scale ULF waves associated with SSC accelerate magnetospheric ultrarelativistic electrons. *Journal of Geophysical Research: Space Physics*, 124, 1525–1538. <https://doi.org/10.1029/2018JA026134>
- Hiraga, R., & Omura, Y. (2020). Acceleration mechanism of radiation belt electrons through interaction with multi-subpacket chorus waves. *Earth Planets and Space*, 72, 21. <https://doi.org/10.1168/s40623-020-1134-3>
- Horne, R. B., & Thorne, R. M. (1998). Potential waves for relativistic electron scattering and stochastic acceleration during magnetic storms. *Geophysical Research Letters*, 25(15), 3011–3014. <https://doi.org/10.1029/98GL01002>
- Horne, R. B., Thorne, R. M., Shprits, Y. Y., Meredith, N. P., Glauert, S. A., Smith, A. J., et al. (2005). Wave acceleration of electrons in the Van Allen radiation belts. *Nature*, 437(7056), 227–230. <https://doi.org/10.1038/nature03939>
- Hsieh, Y.-K., Kubota, Y., & Omura, Y. (2020). Nonlinear evolution of radiation belt electron fluxes interacting with oblique whistler mode chorus emissions. *Journal of Geophysical Research: Space Physics*, 125, e2019JA027465. <https://doi.org/10.1029/2019JA027465>
- Hsieh, Y.-K., & Omura, Y. (2017). Nonlinear dynamics of electrons interacting with oblique whistler mode chorus in the magnetosphere. *Journal of Geophysical Research: Space Physics*, 122, 675–694. <https://doi.org/10.1002/2016JA023255>
- Hudson, M., Jaynes, A., Kress, B., Li, Z., Patel, M., Shen, X.-C., et al. (2017). Simulated prompt acceleration of multi-Mev electrons by the 17 March 2015 interplanetary shock. *Journal of Geophysical Research: Space Physics*, 122, 10036–10046. <https://doi.org/10.1002/2017JA024445>
- Iles, R. H. A., Meredith, N. P., Fazakerley, A. N., & Horne, R. B. (2006). Phase space density analysis of the outer radiation belt energetic electron dynamics. *Journal of Geophysical Research*, 111(A3). <https://doi.org/10.1029/2005JA011206>
- Jaynes, A. N., Baker, D. N., Singer, H. J., Rodriguez, J. V., Loto'aniu, T. M., Ali, A. F., et al. (2015). Source and seed populations for relativistic electrons: Their roles in radiation belt changes. *Journal of Geophysical Research - A: Space Physics*, 120(9), 7240–7254. <https://doi.org/10.1002/2015JA021234>
- Karpman, V. I., & Shklyar, D. R. (1972). Nonlinear damping of potential monochromatic waves in an inhomogeneous plasma. *Soviet Physics Journal of Experimental and Theoretical Physics*, 35, 500.
- Katoh, Y., Omura, Y., & Summers, D. (2008). Rapid energization of radiation belt electrons by nonlinear wave trapping. *Annals of Geophysics*, 26, 3451–3456. <https://doi.org/10.5194/angeo-26-3451-2008>
- Katsavriaias, C., Sandberg, I., Li, W., Podladchikova, O., Daglis, I. A., Papadimitriou, C., et al. (2019). Highly relativistic electron flux enhancement during the weak geomagnetic storm of April–May 2017. *Journal of Geophysical Research: Space Physics*, 124(6), 4402–4413. <https://doi.org/10.1029/2019JA026743>
- Kellerman, A. C., & Shprits, Y. Y. (2012). On the influence of solar wind conditions on the outer-electron radiation belt. *Journal of Geophysical Research*, 117(A5). <https://doi.org/10.1029/2011JA017253>
- Kennel, C. F. (1969). Consequences of a magnetospheric plasma. *Reviews of Geophysics*, 7(1–2), 379–419. <https://doi.org/10.1029/RG007i001p00379>
- Kim, K.-C., Shprits, Y., Subbotin, D., & Ni, B. (2011). Understanding the dynamic evolution of the relativistic electron slot region including radial and pitch angle diffusion. *Journal of Geophysical Research*, 116(A10). <https://doi.org/10.1029/2011JA016684>
- Kletzing, C. A., Kurth, W. S., Acuna, M., MacDowall, R. J., Torbert, R. B., Averkamp, T., et al. (2013). The electric and magnetic field instrument suite and integrated science (EMFISIS) on RBSP. *Space Science Reviews*, 179(1), 127–181. <https://doi.org/10.1007/s11214-013-9993-6>
- Li, X., Roth, I., Temerin, M., Wygant, J. R., Hudson, M. K., & Blake, J. B. (1993). Simulation of the prompt energization and transport of radiation belt particles during the March 24, 1991 SSC. *Geophysical Research Letters*, 20, 2423–2426.
- Li, W., Shprits, Y. Y., & Thorne, R. M. (2007). Dynamic evolution of energetic outer zone electrons due to wave-particle interactions during storms. *Journal of Geophysical Research*, 112(A10). <https://doi.org/10.1029/2007JA012368>
- Lyons, L. R., & Thorne, R. M. (1973). Equilibrium structure of radiation belt electrons. *Journal of Geophysical Research*, 78(13), 2142–2149. <https://doi.org/10.1029/JA078i013p02142>
- Lyons, L. R., Thorne, R. M., & Kennel, C. F. (1972). Pitch-angle diffusion of radiation belt electrons within the plasmasphere. *Journal of Geophysical Research*, 77(19), 3455–3474. <https://doi.org/10.1029/JA077i019p03455>
- Ma, Q., Li, W., Bortnik, J., Thorne, R. M., Chu, X., Ozekte, L. G., et al. (2018). Quantitative evaluation of radial diffusion and local acceleration processes during GEM challenge events. *Journal of Geophysical Research: Space Physics*, 123(3), 1938–1952. <https://doi.org/10.1002/2017JA025114>
- Ma, Q., Li, W., Thorne, R. M., Bortnik, J., Reeves, G. D., Kletzing, C. A., et al. (2016). Characteristic energy range of electron scattering due to plasmaspheric hiss. *Journal of Geophysical Research: Space Physics*, 121(12), 11737–11749. <https://doi.org/10.1002/2016JA023311>
- Ma, Q., Li, W., Thorne, R. M., Ni, B., Kletzing, C. A., Kurth, W. S., et al. (2015). Modeling inward diffusion and slow decay of energetic electrons in the Earth's outer radiation belt. *Geophysical Research Letters*, 42(4), 987–995. <https://doi.org/10.1002/2014GL062977>
- Ma, Q., Li, W., Thorne, R. M., Nishimura, Y., Zhang, X.-J., Reeves, G. D., et al. (2016). Simulation of energy-dependent electron diffusion processes in the Earth's outer radiation belt. *Journal of Geophysical Research: Space Physics*, 121(5), 4217–4231. <https://doi.org/10.1002/2016JA022507>
- Mann, I. R., Ozekte, L. G., Murphy, K. R., Claudepierre, S. G., Turner, D. L., Baker, D. N., et al. (2016). Explaining the dynamics of the ultra-relativistic third Van Allen radiation belt. *Nature Physics*, 12(10), 978–983. <https://doi.org/10.1038/nphys3799>
- Millan, R. M., Lin, R. P., Smith, D. M., & McCarthy, M. P. (2007). Observation of relativistic electron precipitation during a rapid decrease of trapped relativistic electron flux. *Geophysical Research Letters*, 34(10). <https://doi.org/10.1029/2006GL028653>
- Nunn, D. (1971). Wave-particle interactions in electrostatic waves in an inhomogeneous medium. *Journal of Plasma Physics*, 6, 291. <https://doi.org/10.1017/S0022377800006061>
- Omura, Y., Furuya, N., & Summers, D. (2007). Relativistic turning acceleration of resonant electrons by coherent whistler mode waves in a dipole magnetic field. *Journal of Geophysical Research*, 112, A06236. <https://doi.org/10.1029/2006JA012243>
- Omura, Y., Hsieh, Y.-K., Foster, J. C., Erickson, P. J., Kletzing, C. A., & Baker, D. N. (2019). Cyclotron acceleration of relativistic electrons through Landau resonance with obliquely propagating whistler-mode chorus emissions. *Journal of Geophysical Research: Space Physics*, 124, 2795–2810. <https://doi.org/10.1029/2018JA026374>
- Omura, Y., Miyashita, Y., Yoshikawa, M., Summers, D., Hikishima, M., Ebihara, Y., & Kubota, Y. (2015). Formation process of relativistic electron flux through interaction with chorus emissions in the Earth's inner magnetosphere. *Journal of Geophysical Research*, 120, 9545–9562. <https://doi.org/10.1002/2015JA021563>
- Orlova, K., & Shprits, Y. (2014). Model of lifetimes of the outer radiation belt electrons in a realistic magnetic field using realistic chorus wave parameters. *Journal of Geophysical Research: Space Physics*, 119(2), 770–780. <https://doi.org/10.1002/2013JA019596>
- Orlova, K., Shprits, Y., & Spasojevic, M. (2016). New global loss model of energetic and relativistic electrons based on Van Allen Probes measurements. *Journal of Geophysical Research: Space Physics*, 121(2), 1308–1314. <https://doi.org/10.1002/2015JA021878>
- Orlova, K., Spasojevic, M., & Shprits, Y. (2014). Activity-dependent global model of electron loss inside the plasmasphere. *Geophysical Research Letters*, 41(11), 3744–3751. <https://doi.org/10.1002/2014GL060100>

- Qin, M., Hudson, M., Li, Z., Millan, R., Shen, X., Shprits, Y., et al. (2019). Investigating loss of relativistic electrons associated with EMIC waves at low L values on 22 June 2015. *Journal of Geophysical Research: Space Physics*, 124(6), 4022–4036. <https://doi.org/10.1029/2018JA025726>
- Reeves, G. D., Baker, D. N., Belian, R. D., Blake, J. B., Cayton, T. E., Fennell, J. F., et al. (1998). The global response of relativistic radiation belt electrons to the January 1997 magnetic cloud. *Geophysical Research Letters*, 25(17), 3265–3268. <https://doi.org/10.1029/98GL02509>
- Reeves, G. D., Spence, H. E., Henderson, M. G., Morley, S. K., Friedel, R. H. W., Funsten, H. O., et al. (2013). Electron acceleration in the heart of the van allen radiation belts. *Science*, 341(6149), 991–994. <https://doi.org/10.1126/science.1237743>
- Ripoll, J.-F., Loridan, V., Denton, M. H., Cunningham, G., Reeves, G., Santolik, O., et al. (2019). Observations and Fokker-Planck simulations of the L-shell, energy, and pitch angle structure of Earth's electron radiation belts during quiet times. *Journal of Geophysical Research: Space Physics*, 124(2), 1125–1142. <https://doi.org/10.1029/2018JA026111>
- Ripoll, J.-F., Reeves, G. D., Cunningham, G. S., Loridan, V., Denton, M., Santolik, O., et al. (2016). Reproducing the observed energy-dependent structure of Earth's electron radiation belts during storm recovery with an event-specific diffusion model. *Geophysical Research Letters*, 43(11), 5616–5625. <https://doi.org/10.1002/2016GL068869>
- Rodger, C. J., Hendry, A. T., Clilverd, M. A., Kletzing, C. A., Brundell, J. B., & Reeves, G. D. (2015). High-resolution in situ observations of electron precipitation-causing EMIC waves. *Geophysical Research Letters*, 42, 9633. <https://doi.org/10.1002/2015GL066581>
- Sandanger, M., Søraas, F., Sørø, M., Aarsnes, K., Oksavik, K., & Evans, D. (2009). Relativistic electron losses related to EMIC waves during CIR and CME storms. *Journal of Atmospheric and Solar-Terrestrial Physics*, 71(10–11), 1126–1144. <https://doi.org/10.1016/j.jastp.2008.07.006>
- Schulz, M., & Lanzerotti, L. J. (1974). *Particle diffusion in the radiation belts* (Vol. 7). Springer Science & Business Media.
- Selesnick, R. S., & Blake, J. B. (2000). On the source location of radiation belt relativistic electrons. *Journal of Geophysical Research*, 105(A2), 2607. <https://doi.org/10.1029/1999JA900445>
- Shapiro, V. D., & Sagdeev, R. Z. (1997). Nonlinear wave-particle interaction and conditions for the applicability of quasilinear theory. *Physics Reports*, 283, 49–71. [https://doi.org/10.1016/S0370-1573\(96\)00053-1](https://doi.org/10.1016/S0370-1573(96)00053-1)
- Sheeley, B. W., Moldwin, M. B., Rassoul, H. K., & Anderson, R. R. (2001). An empirical plasmasphere and trough density model: CRRES observations. *Journal of Geophysical Research*, 106(A11), 25631–25641. <https://doi.org/10.1029/2000JA000286>
- Shklyar, D., & Matsumoto, H. (2009). Oblique whistler-mode waves in the inhomogeneous magnetospheric plasma: Resonant interactions with energetic charged particles. *Surveys in Geophysics*, 30, 55–104. <https://doi.org/10.1007/s10712-009-9061-7>
- Shprits, Y. Y., Chen, L., & Thorne, R. M. (2009). Simulations of pitch angle scattering of relativistic electrons with MLT-dependent diffusion coefficients. *Journal of Geophysical Research*, 114(A3). <https://doi.org/10.1029/2008JA013695>
- Shprits, Y. Y., Drozdov, A. Y., Spasojevic, M., Kellerman, A. C., Usanova, M. E., Engebretson, M. J., et al. (2016). Wave-induced loss of ultra-relativistic electrons in the Van Allen radiation belts. *Nature Communications*, 7(1), 12883. <https://doi.org/10.1038/ncomms12883>
- Shprits, Y. Y., Horne, R. B., Kellerman, A. C., & Drozdov, A. Y. (2018). The dynamics of Van Allen belts revisited. *Nature Physics*, 14(2), 102–103. <https://doi.org/10.1038/nphys4350>
- Shprits, Y. Y., Kellerman, A., Aseev, N., Drozdov, A. Y., & Michaelis, I. (2017). Multi-MeV electron loss in the heart of the radiation belts. *Geophysical Research Letters*, 44(3), 1204–1209. <https://doi.org/10.1002/2016GL072258>
- Shprits, Y. Y., & Ni, B. (2009). Dependence of the quasi-linear scattering rates on the wave normal distribution of chorus waves. *Journal of Geophysical Research*, 114(A11). <https://doi.org/10.1029/2009JA014223>
- Shprits, Y. Y., Subbotin, D., Drozdov, A., Usanova, M. E., Kellerman, A., Orlova, K., et al. (2013). Unusual stable trapping of the ultrarelativistic electrons in the Van Allen radiation belts. *Nature Physics*, 9(11), 699–703. <https://doi.org/10.1038/nphys2760>
- Shprits, Y. Y., Subbotin, D. A., Meredith, N. P., & Elkington, S. R. (2008). Review of modeling of losses and sources of relativistic electrons in the outer radiation belt II: Local acceleration and loss. *Journal of Atmospheric and Solar-Terrestrial Physics*, 70(14), 1694–1713. <https://doi.org/10.1016/j.jastp.2008.06.014>
- Shprits, Y. Y., & Thorne, R. M. (2004). Time dependent radial diffusion modeling of relativistic electrons with realistic loss rates. *Geophysical Research Letters*, 31(8). <https://doi.org/10.1029/2004GL019591>
- Shprits, Y. Y., Thorne, R. M., Friedel, R., Reeves, G. D., Fennell, J., Baker, D. N., & Kanekal, S. G. (2006). Outward radial diffusion driven by losses at magnetopause. *Journal of Geophysical Research*, 111(A11). <https://doi.org/10.1029/2006JA011657>
- Shprits, Y. Y., Thorne, R. M., Horne, R. B., Glauert, S. A., Cartwright, M., Russell, C. T., et al. (2006). Acceleration mechanism responsible for the formation of the new radiation belt during the 2003 Halloween solar storm. *Geophysical Research Letters*, 33(5). <https://doi.org/10.1029/2005GL024256>
- Shprits, Y. Y., Thorne, R. M., Reeves, G. D., & Friedel, R. (2005). Radial diffusion modeling with empirical lifetimes: Comparison with CRRES observations. *Annals of Geophysics*, 23(4), 1467–1471. <https://doi.org/10.5194/angeo-23-1467-2005>
- Shue, J.-H., Chao, J. K., Fu, H. C., Russell, C. T., Song, P., Khurana, K. K., & Singer, H. J. (1997). A new functional form to study the solar wind control of the magnetopause size and shape. *Journal of Geophysical Research*, 102(A5), 9497–9511. <https://doi.org/10.1029/97JA00196>
- Streltsov, A. V., Lampe, M., Manheimer, W., Ganguli, G., & Joyce, G. (2006). Whistler propagation in inhomogeneous plasma. *Journal of Geophysical Research*, 111, A03216. <https://doi.org/10.1029/2005JA011357>
- Su, Z., Xiao, F., Zheng, H., He, Z., Zhu, H., Zhang, M., et al. (2014). Nonstorm time dynamics of electron radiation belts observed by the Van Allen Probes. *Geophysical Research Letters*, 41(2), 229–235. <https://doi.org/10.1002/2013GL058912>
- Subbotin, D. A., & Shprits, Y. Y. (2009). Three-dimensional modeling of the radiation belts using the Versatile Electron Radiation Belt (VERB) code. *Space Weather*, 7(10). <https://doi.org/10.1029/2008SW000452>
- Subbotin, D. A., Shprits, Y., & Ni, B. (2010). Three-dimensional VERB radiation belt simulations including mixed diffusion. *Journal of Geophysical Research*, 115(A3). <https://doi.org/10.1029/2009JA015070>
- Summers, D. A., & Omura, Y. (2007). Ultra-relativistic acceleration of electrons in planetary magnetospheres. *Geophysical Research Letters*, 34, L24205. <https://doi.org/10.1029/2007GL032226>
- Summers, D. A., & Thorne, R. M. (2003). Relativistic electron pitch-angle scattering by electromagnetic ion cyclotron waves during geomagnetic storms. *Journal of Geophysical Research*, 108(A4). <https://doi.org/10.1029/2002JA009489>
- Summers, D. A., Thorne, R. M., & Xiao, F. (1998). Relativistic theory of wave-particle resonant diffusion with application to electron acceleration in the magnetosphere. *Journal of Geophysical Research*, 103(A9), 20487–20500. <https://doi.org/10.1029/98JA01740>
- Thorne, R. M., & Kennel, C. F. (1971). Relativistic electron precipitation during magnetic storm main phase. *Journal of Geophysical Research*, 76(19), 4446–4453. <https://doi.org/10.1029/IA076i019p04446>
- Thorne, R. M., Li, W., Ni, B., Ma, Q., Bortnik, J., Chen, L., et al. (2013). Rapid local acceleration of relativistic radiation-belt electrons by magnetospheric chorus. *Nature*, 504(7480), 411–414. <https://doi.org/10.1038/nature12889>
- Thorne, R. M., O'Brien, T. P., Shprits, Y. Y., Summers, D., & Horne, R. B. (2005). Timescale for MeV electron microburst loss during geomagnetic storms. *Journal of Geophysical Research*, 110(A9). <https://doi.org/10.1029/2004JA010882>

- Tsyganenko, N. A. (1989). A magnetospheric magnetic field model with a warped tail current sheet. *Planetary and Space Science*, 37(1), 5–20. [https://doi.org/10.1016/0032-0633\(89\)90066-4](https://doi.org/10.1016/0032-0633(89)90066-4)
- Tsyganenko, N. A., & Sitnov, M. I. (2005). Modeling the dynamics of the inner magnetosphere during strong geomagnetic storms. *Journal of Geophysical Research*, 110(A3). <https://doi.org/10.1029/2004JA010798>
- Tsyganenko, N. A., & Sitnov, M. I. (2007). Magnetospheric configurations from a high-resolution data-based magnetic field model. *Journal of Geophysical Research*, 112(A6). <https://doi.org/10.1029/2007JA012260>
- Tu, W., Cunningham, G. S., Chen, Y., Henderson, M. G., Camporeale, E., & Reeves, G. D. (2013). Modeling radiation belt electron dynamics during GEM challenge intervals with the DREAM3D diffusion model. *Journal of Geophysical Research: Space Physics*, 118(10), 6197–6211. <https://doi.org/10.1002/jgra.50560>
- Turner, D. L., Shprits, Y., Hartinger, M., & Angelopoulos, V. (2012). Explaining sudden losses of outer radiation belt electrons during geomagnetic storms. *Nature Physics*, 8(3), 208–212. <https://doi.org/10.1038/nphys2185>
- Ukhorskiy, A. Y., Shprits, Y. Y., Anderson, B. J., Takahashi, K., & Thorne, R. M. (2010). Rapid scattering of radiation belt electrons by storm-time EMIC waves. *Geophysical Research Letters*, 37(9). <https://doi.org/10.1029/2010GL042906>
- Ukhorskiy, A. Y., Sitnov, M., Mitchell, D., Takahashi, K., Lanzerotti, L. J., & Mauk, B. H. (2014). Rotationally driven ‘zebra stripes’ in Earth’s inner radiation belt. *Nature*, 507, 338–340. <https://doi.org/10.1038/nature13046>
- Usanova, M. E., Drozdov, A., Orlova, K., Mann, I. R., Shprits, Y., Robertson, M. T., et al. (2014). Effect of EMIC waves on relativistic and ultra-relativistic electron populations: Ground-based and Van Allen Probes observations. *Geophysical Research Letters*, 41(5), 1375–1381. <https://doi.org/10.1002/2013GL059024>
- Varotsou, A., Boscher, D., Bourdarie, S., Horne, R. B., Meredith, N. P., Glauert, S. A., & Friedel, R. H. (2008). Three-dimensional test simulations of the outer radiation belt electron dynamics including electron-chorus resonant interactions. *Journal of Geophysical Research*, 113(A12). <https://doi.org/10.1029/2007JA012862>
- Walt, M. (1994). *Introduction to geomagnetically trapped radiation*. Cambridge University Press.
- Wang, D., & Shprits, Y. Y. (2019). On how high-latitude chorus waves tip the balance between acceleration and loss of relativistic electrons. *Geophysical Research Letters*, 46(14), 7945–7954.
- Wang, D., Shprits, Y. Y., Zhelavskaya, I., Agapitov, O., Drozdov, A., & Aseev, N. (2019). Analytical chorus wave model derived from Van Allen Probe observations. *Journal of Geophysical Research: Space Physics*, 124, 1063–1084. <https://doi.org/10.1029/2018JA026183>
- Wang, D., Shprits, Y. Y., Zhelavskaya, I. S., Effenberger, F., Castillo, A., Drozdov, A. Y., et al. (2020). The effect of plasma boundaries on the dynamic evolution of relativistic radiation belt electrons. *Journal of Geophysical Research: Space Physics*, e2019JA027422. <https://doi.org/10.1029/2019JA027422>
- Woodger, L. A., Halford, A. J., Millan, R. M., McCarthy, M. P., Smith, D. M., Bowers, G. S., et al. (2015). A summary of the BARREL campaigns: Technique for studying electron precipitation. *Journal of Geophysical Research: Space Physics*, 120(6), 4922–4935. <https://doi.org/10.1002/2014JA020874>
- Woodger, L. A., Millan, R. M., Li, Z., & Sample, J. G. (2018). Impact of background magnetic field for emic wave-driven electron precipitation. *Journal of Geophysical Research: Space Physics*, 123(10), 8518–8532. <https://doi.org/10.1029/2018ja025315>
- Zhao, H., Baker, D. N., Li, X., Malaspina, D. M., Jaynes, A. N., & Kanekal, S. G. (2019). On the acceleration mechanism of ultrarelativistic electrons in the center of the outer radiation belt: A statistical study. *Journal of Geophysical Research: Space Physics*, 124(11), 8590–8599. <https://doi.org/10.1029/2019JA027111>
- Zhelavskaya, I. S., Spasojevic, M., Shprits, Y. Y., & Kurth, W. S. (2016). Automated determination of electron density from electric field measurements on the Van Allen Probes spacecraft. *Journal of Geophysical Research: Space Physics*, 121(5), 4611–4625. <https://doi.org/10.1002/2015JA022132>
- Zong, Q.-G., Zhou, X.-Z., Wang, Y. F., Li, X., Song, P., Baker, D. N., et al. (2009). Energetic electrons response to ULF waves induced by interplanetary shocks in the outer radiation belt. *Journal of Geophysical Research*, 114, A10204. <https://doi.org/10.1029/2009JA014393>